Title

Correlated Electron Behavior in Single Crystals Grown by Molten Metal Flux : : MnAs and $Ce_{1-x}Yb_xCoIn_5$

Permalink

https://escholarship.org/uc/item/008997wj

Author

Lum, Ivy

Publication Date

2014

Peer reviewed|Thesis/dissertation

UNIVERSITY OF CALIFORNIA, SAN DIEGO

Correlated Electron Behavior in Single Crystals Grown by Molten Metal Flux: MnAs and $Ce_{1-x}Yb_xCoIn_5$

A thesis submitted in partial satisfaction of the
requirements for the degree Master of Science
in
Materials Science and Engineering

by

Ivy Lum

Committee in charge:

Professor M. Brian Maple, Chair
Professor Eric Fullerton
Professor Vitale F. Nesterenko

2014

The thesis of Ivy Lum is approved, and it is acceptable in quality and form for publication on microfilm and electronically:

Chair

University of California, San Diego

2014

I dedicate this to my loving family who continue to support this chaotic life of mine. Also, to all of those who always gave me unyielding patience and advice, I thank you. Duygu and Sooyoung, simply put, I will miss you. Kevin and Colin, you will always be my academic big brothers. You taught me then worked with me, laughed with me and vented with me, all the while feeding me kernels of knowledge. As an undergraduate, you taught me an unfamiliar type of research, a bridge between physics and chemistry called condensed matter, and truly changed my path in life. I will cherish the memories we created and I will always be grateful. John, you are my rock. You are the reason I can smile every day. Your influence makes me a better person.

The art of war is simple enough.
Find out where your enemy is.
Get at him as soon as you can.
Strike him as hard as you can,
and keep moving on.
–Ulysses. S Grant

Every day you may make progress. Every step may be fruitful.
Yet there will stretch out before you an ever-lengthening, ever-ascending,
ever-improving truth. You know you will never get to the end of the journey. But
this, so far from discouraging, only adds to the joy and glory of the climb.
– Sir Winston Churchill

Mistakes are part of being human. Appreciate your mistakes for what they are:
precious life lessons that can only be learned the hard way. Unless it's a fatal
mistake, which, at least, others can learn from.
– Al Franken

We must learn to manage our ignorance.
– M. Brian Maple

TABLE OF CONTENTS

LIST OF FIGURES

LIST OF TABLES

ACKNOWLEDGEMENTS

My gratitude to everyone for believing that I will finish on time and giving me the space to do so. I would like to thank Dr. Brian Maple for entrusting me with important synthesis for collaborators; trusting a graduate student to create high quality materials for others cannot be a stress-free endeavor. I would also like to thank my mentors: Dr. Ryan Baumbach, Dr. Marc Janoschek, and Dr. James Hamlin. Without the many lessons, tricks of the trade and numerous discussions shared, life would have been boring and unproductive. To Dr. Ben White and Dr. Noravee Kanchanavatee, thank you for your insights. You made Random Question Fridays much more interesting. It has been a pleasure and an honor to work with both of you. Aaron, thank you for all the work on the various projects over the years. I know I had you perform some oddly specific tasks and I thank you for accepting my quirks.

This research in this thesis was sponsored by the U.S. Department of Energy (DOE) under Research Grant # DE-FG02-04ER46105 and by the National Science Foundation under Grant No. DMR 0802478. The crystal growth work reported in this thesis was sponsored by the U.S. Department of Energy (DOE) under Research Grant # DE FG02-04ER46178. Sponsorship was granted by Quantum Design through the Ron Sager Young Scientist Scholarship.

VITA

2014	Master of Science in Materials Science and Engineering University of California, San Diego
2009-2012	Laboratory Assistant, University of California, San Diego
2009	Bachelor of Science in Physics, University of California, San Diego

PUBLICATIONS

R.E. Baumbach, J.J. Hamlin, M. Janoschek, I.K. Lum and M.B. Maple, Magnetic, thermal, and transport properties of the actinide based noncentrosymmetric compounds $\mathrm{The_2Fe_12P_7}$ and $\mathrm{U_2Fe_12P_7}$, J. Phys.: Condens. Matter **23**, 094222 (2011).

M. Janoschek, R. E. Baumbach, J. J. Hamlin, I. K. Lum and M. B. Maple, The noncentrosymmetric heavy fermion ferromagnet $\mathrm{Sm_2Fe_12P_7}$, J. Phys.: Condens. Matter **23**, 094221 (2011).

D. A. Zocco, R. E. Baumbach, J. J. Hamlin, M. Janoschek, I. K. Lum, M. A. McGuire, A. S. Sefat, B. C. Sales, R. Jin, D. Mandrus, J. R. Jeffries, S. T. Weir, Y. K. Vohra and M. B. Maple, Search for pressure induced superconductivity in CeFeAsO and CeFePO iron pnictides, Phys. Rev. B **83**, 094528 (2011).

R. E. Baumbach, J. J. Hamlin, P.-C. Ho, I. K. Lum and M. B. Maple, Anisotropy in the superconductivity and magnetism of LnFePO (Ln= La, Pr and Nd), Physical Review B **85**, 104526 (2012).

B. D. White, J. J. Hamlin, K. Huang, I. K. Lum, R. E. Baumbach, M. Janoschek, and M. B. Maple, Insensitivity of the pressure dependences of characteristic energy scales in $\mathrm{Ce}_(1-x)\mathrm{R}_x\mathrm{CoIn}_5$ (R = Yb, Y, Gd0 to the electronic configuration of the rare-earth ion, Phys. Rev. B **86**, 100502(R) (2012).

B. D. White, M. Janoschek, N. Kanchanavatee, K. Huang, L. Shu, S. Jang, D. Y. Tutun, J.J. Hamlin, I. K. Lum, R. E. Baumbach and M. B. Maple, Thermoelectric properties of correlated electron systems $\mathrm{Ln_3Pt_4Ge_6}$ and $\mathrm{LnPt_4Ge_12}$ (Ln = Ce, Pr) and non-centrosymmetric $\mathrm{X_2T_12P_7}$ (X = Yb, Hf, and T = Fe, Co), New Materials for Thermoelectric Applications: Theory and Experiment, [Proceedings of the NATO Advanced Research Workshop on New Materials for Thermoelectric Applications: Theory and Experiment], Hvar, Croatia, Sept. 19-25, 2011 (2013), 31-43

N. J. Hillier, N. Foroozani, D. A. Zocco, J. J. Hamlin, R. E. Baumbach, I. K. Lum, M. B. Maple, J. S. Schilling, Intrinsic dependence of Tc on hydrostatic (He-gas) pressure for superconducting LaFePO, PrFePO, and NdFePO single crystals, Physical Review B: Condensed Matter and Materials Physics (2012), **86** (21), 214517

N. Foroozani, J. J. Hamlin, J. S. Schilling, R. E. Baumbach, I. K. Lum, L. Shu, K. Huang, M. B. Maple, Dependence of the superconducting transition temperature of the filled skutterudite compound $\mathrm{PrPt_4Ge_1 2}$ on hydrostatic pressure, Physica C: Superconductivity and Its Applications (Amsterdam, Netherlands) (2013), **485**, 160-162.

D. Yazici, K. Huang, B. D. White, I. Jeon, V. W. Burnett, A. J. Friedman,I. K. Lum, M. Nallaiyan, S. Spagna, M. B. Maple, Superconductivity induced by electron doping in the system $\mathrm{La}_(1-x)\mathrm{M}_x\mathrm{OBiS}_2$ (M= Ti, Zr, Hf, Th), arXiv.org, e-Print Archive, Condensed Matter (2013), 1-7, arXiv:1303.6216v1

K. Huang, L. Shu, I. K. Lum, B. D. White, M. Janoschek, D. Yazici, J.J. Hamlin, D. A. Zocco, P.-C. Ho, R. E. Baumbach, et al Probing the superconductivity of $\mathrm{PrPt_4Ge_1 2}$ through Ce substitution Physical Review B: Condensed Matter and Materials Physics (2014), **89** (3), 035145

Hyunsoo Kim, M. A. Tanatar, R. Flint, C. Petrovic, Rongwei Hu, B. D. White, I. K. Lum, M. B. Maple and R. Prozorov, Evolution of the superconducting energy gap structure concomitant with Fermi surface reconstruction in the heavy-fermion superconductor $\mathrm{CeCoIn_5}$, arXiv.org, e-Print Archive, Condensed Matter (2014), 1-6, arXiv:1404.3700v1

Y. P. Singh, D. J. Haney, X. Y. Huang, I. K. Lum, B. D. White, M. Dzero, M. B. Maple, C. C. Almasan, From local moment to mixed-valence regime in $\mathrm{Ce}_(1-x)\mathrm{Yb}_x\mathrm{CoIn}_5$ alloys, Physical Review B: Condensed Matter and Materials Physics (2014), **89** (11), 115106

Summary of exploratory synthesis efforts in superconductivity search under the AFOSR-MURI program, Presented at 2011 Superconductivity Program Review and USAF-China Workshop, Santa Barbara, California, USA, December 12- 15, 2011. (poster)

B. D. White, K. Huang, I. K. Lum, J. J. Hamlin, S. Jang, G. J. Smith, J. W. Simonson, C. S. Nelson, M. C. Aronson, and M. B. Maple, ”Physical Properties of MnAs single crystals grown in molten Sn flux,” submitted May 2014

FIELDS OF STUDY

Major Field: Materials Science and Engineering
Studies in strongly correlated electron materials
M. Brian Maple, Bernd T. Matthias Professor of Physics,
University of California, San Diego

ABSTRACT OF THE THESIS

Correlated Electron Behavior in Single Crystals Grown by Molten Metal Flux:
MnAs and $Ce_{1-x}Yb_xCoIn_5$

by

Ivy Lum
Master of Science in Materials Science and Engineering
University of California, San Diego, 2014
Professor M. Brian Maple

Investigations into flux techniques for producing reliable and consistent single crystals were conducted for ongoing studies on correlated electrons systems: MnAs, $Ce_{(1-x)}Yb_xCoIn_5$, and $La_{(1-x)}M_xOBiS_2$. MnAs, as a potential candidate for energy efficient materials, has been recently synthesized in bulk, single crystals to understand the nature of the magnetocaloric effect and its correlation to potential magnetic refrigeration techniques. Single crystals were grown in a molten metal flux and characterization focused on the first and second order transitions. $CeCoIn_5$ has received a great deal of attention in recent years due to its exotic normal state behavior and possibly magnetically mediated superconductivity. Ytterbium was substituted into parent compound $CeCoIn_5$ to assist in the ongoing investigations into the potential valence transition with increasing Yb located at the Cerium sites. A reinterpretation of the valence fluctuations and cooperations based off previous measurements is suggested. Characterization was performed at temperatures down to 0.36 K at Quantum Design for the compound $La_{(1-x)}M_xOBiS_2$.

I

Introduction

Investigations into synthesis techniques for producing reliable and consistent single crystals for ongoing studies in both low temperature and high temperature regimes. Investigations into the exchange interactions of single crystals compounds grown by molten metal flux growth. MnAs, as a potential candidate for energy efficient materials due to its “colossal magnetoresistance, has been recently re-investigated in various forms and scales to better understand the nature of the magnetocaloric effect and its correlation to potential magnetic refrigeration techniques. It has also been shown that materials based on MnAs present a significant energy loss during a temperature cycle due to their high thermal hysteresis, and therefore, they would have limited technological application. Single crystals were grown in a molten metal flux with characterization focusing on the first and second order transitions. $CeCoIn_5$ has received a great deal of attention in recent years due to its exotic normal state behavior and possibly magnetically mediated superconductivity. Ytterbium was substituted into parent compound $CeCoIn_5$to assist in the ongoing investigations into the potential valence transition with increasing Yb located at the Cerium sites and a reinterpretation of previous measurements is suggested. However, before divulging the results of the investigations the conceptual foundation must be put forth.

I.A Magnetism

Magnetism is a heavily studied topic in correlated electron systems. The magnetic moments of a free atom can be attributed to its spin (S), orbital angular momentum (L), and the orbital angular momentum induced by an applied field. Magnetization, M, is defined as the magnetic moment per unit volume and the magnetic susceptibility, χ, of a free atom is defined as:

$$\chi = \frac{M}{H} \tag{I.1}$$

where H is the macroscopic magnetic field. There are at least two scenarios in which electrons can contribute to the magnetization of a compound. Figure I.1 illustrates magnetic interactions via simple models. The electrons or holes that contribute to a compound are localized electrons are restricted to the space around the associated atom. Only the local electrons in unfilled shells contribute a magnetic moment. A second scenario are the electrons located in the conduction band, also known as itinerant electrons. They are not restricted to the host atoms but travel freely throughout the compound. The systems investigated in this thesis have enhanced correlations between the localized and conduction electrons, potentially leading to hybridization. An important distinction between the two types of electrons are the magnetic moments of each. Recall that for local electrons, both orbital and spin angular momentum contribute to the magnetic moment. For itinerant electrons this is no longer the case. Since itinerant electrons do not necessarily orbit around an ion they typically have no orbital angular momentum. Only the intrinsic spin of the electron contributes to a magnetic moment of an itinerant electron [26].

I.A.1 Diamagnetism

In a diamagnetic material, a magnetic field induces a magnetic moment which opposes the applied magnetic field. A diamagnetic response is found in materials which contains only paired electrons and thus no magnetic moment unless

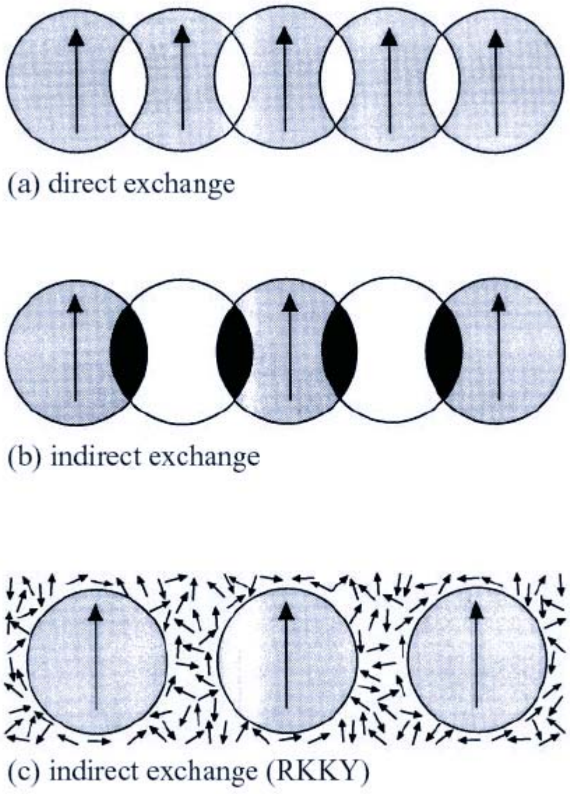

Figure I.1: Simple models of magnetic exchange interactions [26]

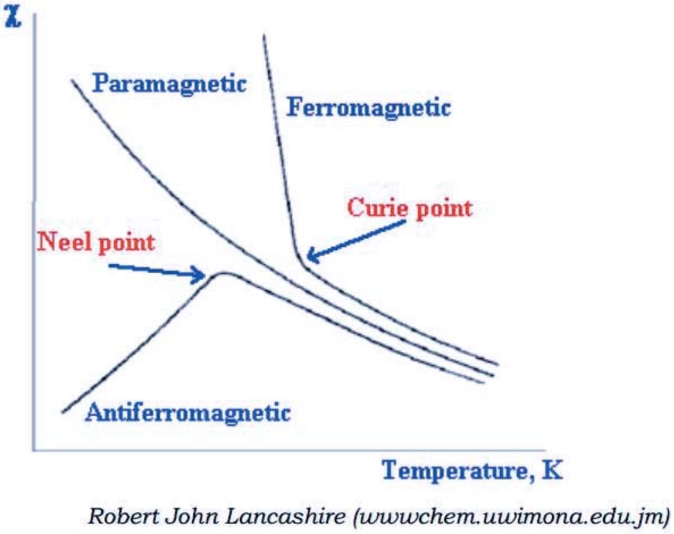

Figure I.2: Simple diagram of temperature dependent magnetisms. Redrawn after a model created by Robert Lancashire (website shown)

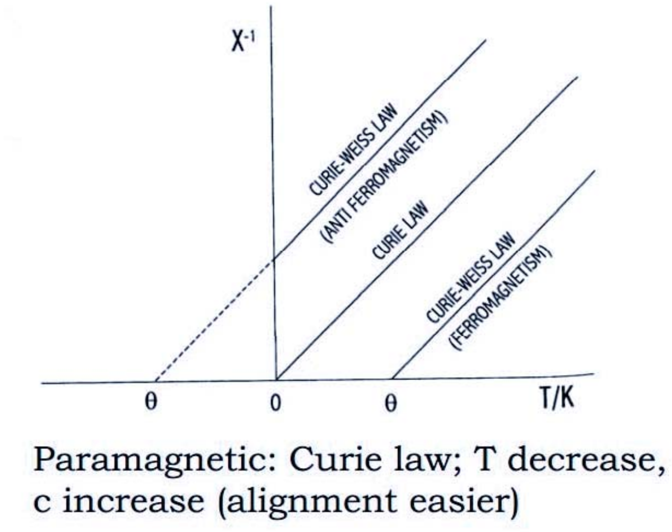

Figure I.3: Curie law dependence of the magnetic susceptibility for a paramagnet, where $\chi \propto 1/\mathrm{T}$. This results in a linear $1/\chi$ vs. T [49]

a field is applied. When a field is applied, the electrical charges tend to shield the interior of the body resulting in a change of magnetic flux within the system. The induced current creates its own magnetic field opposing the applied field, in direction and intensity, mostly. While diamagnetism is temperature independent and present in all materials to some degree, it is only easily detected in materials that do not contain a permanent magnetic moment [8]. Superconductors are examples of perfect diamagnets which completely expel applied field and have an explanation in Section I.C.

I.A.2 Paramagnetism

Paramagnetic materials typically have weakly interacting permanent magnetic moments due to unpaired electrons and/or unfilled electron orbitals. Without an applied field, the magnetic moments are randomly oriented, but still produces a net moment/magnetization. When a field is applied the atomic dipoles align parallel with the applied field slightly strengthening the field. The magnetic moment is associated with the total angular momentum, J, as the sum of the orbital angular momentum, L, and the spin, S, shown in the following equation:

$$J = L + S \tag{I.2}$$

A true paramagnet should show no signs of magnetic ordering down to the lowest temperature and its magnetization should vary inversely with temperature as well as an applied magnetic field. For low magnetic fields and high temperatures, when the moments are not entirely aligned, the susceptibility of a paramagnet follows the Curie law:

$$\chi = \frac{C}{T} = \frac{(\mu_0 \mu_{eff}^2)}{k_B T} \tag{I.3}$$

where C is the Curie constant, μ_{eff} is the effective magnetic moment, μ_0 is the permeability of free space, k_B is Boltzmann's constant [8]. The effective magnetic moment is characterized by the total angular momentum J where

$$\mu_{eff} = g_J \sqrt{J(J+1)} \mu_B \tag{I.4}$$

where, g_J is the Lande factor. In higher fields and lower temperatures, the magnetization is no longer linear in temperature and the Curie Law no longer holds under these circumstances. Schematic behavior of χ for paramagnetic material verses temperature T(K) in low field with decreasing temperature is shown in fig. I.3. In some metals, Pauli paramagnetism, paramagnetism of free electrons, is seen and is characterized by nearly temperature independent susceptibility as seen in $\mathrm{YbCoIn_5}$ [10]. For itinerant electrons, when applying a magnetic field, there is a slight splitting of the energy levels of the conduction band. An important note about the magnetic susceptibility χ of Pauli paramagnetism is that it is very temperature independent. In paramagnetism of local electrons, each ion contributes an electron while in Pauli paramagnetism only the electrons on the Fermi surface contribute therefore Pauli paramagnetism is negligible compared to paramagnetism [8].

I.A.3 Ferromagnetism

Ferromagnetism occurs when the spins spontaneously align parallel with each other below the critical temperature, T_C. At high temperatures, $T > T_C$, the behavior of the spin angular momentum of a ferromagnet (and therefore the magnetic moment) is that of a paramagnet. This is due to the high thermal fluctuations of the electrons which randomly orient the magnetic moments. The characteristic temperature which splits the two regions apart (order or disorder) is known as the Curie temperature, T_C. Above the Curie temperature the solid behaves as a paramagnet and is characterized by the Curie-Weiss law:

$$\chi = \frac{C}{T - \theta_{CW}} \tag{I.5}$$

where the new term, θ_{CW} is the paramagnetic Curie temperature. For simple ferromagnets, θ_{CW} is equal to the Curie temperature, T_C . Once the temperature drops below the Curie temperature, the magnetic moments of the solid spontaneously align parallel to each other, even in the absence of an external magnetic field. Therefore below the Curie temperature, the magnetic susceptibility can no longer be represented by the Curie-Weiss law [8].

Metals and systems where there are mainly conduction electrons can also order ferromagnetically. This scenario is referred to as itinerant ferromagnetism and is analogous to weak ferromagnetism. Recall from previous sections that because conduction electrons do not have orbital angular momentum, their magnetic moments are small, resulting in a decreased magnetization of the compound. Therefore, the magnetization of itinerant ferromagnets are much lower than ferromagnetism in localized electrons. For cases where the interactions between the localized electrons are strong, long-range ordering can occur. The exchange interaction can be thought of as the spin angular momentums of two electrons correlated by an exchange coefficient. When the exchange coefficient is positive, the energy is lowered when the spin angular momentum of the two electrons align. Since nature favors the lowest energetic state, the solid will be most stable with the moments aligned parallel to each other.

I.A.4 Antiferromagnetism

When the exchange interaction coefficient is negative the two electrons spin angular momentums will align antiparallel with each other. The nearest electron neighbors see the change in states of the spins and rearrange themselves producing an effective net momentum of zero. The magnetic susceptibility at high temperatures obeys the Curie-Weiss law, however, below the characteristic temperature, now called the Neel temperature (T_N), the magnetization drops. The parameter θ is negative for antiferromagnets but is not equal to T_N.

I.B Magnetoresistance and Magnetocaloric Effect

I.B.1 Magnetoresistance

Magnetoresistance (MR) is the change of a material's resistivity with the application of a magnetic field and is a well known phenomenon whose origins lie in spin orbit coupling. The electron cloud surrounding the nucleus will deform under a rotating applied field causing a change in scattering as the itinerant electrons traverse the lattice. If the field and the magnetization are oriented transverse to the induced current then the electron orbitals are in the current plane and a low resistive state is achieved. Conversely, if the field is parallel to the current plane the orbitals are perpendicular and the cross-section capable of scattering is increased leading to an increase in the resistance [41]. This is the basic concept behind spintronics and can be greatly manipulated by design as can be seen in Fig. I.4.

Magnetoresistive materials fit into one of four categories: ordinary MR, anisotropic MR, giant MR and colossal MR. These are separated by the scaling of $\frac{\Delta\rho}{(\rho)}$. Ordinary MR candidates typically include pure elements and have very small ratios independent of crystallographic orientation [38]. Anisotropic MR candidates

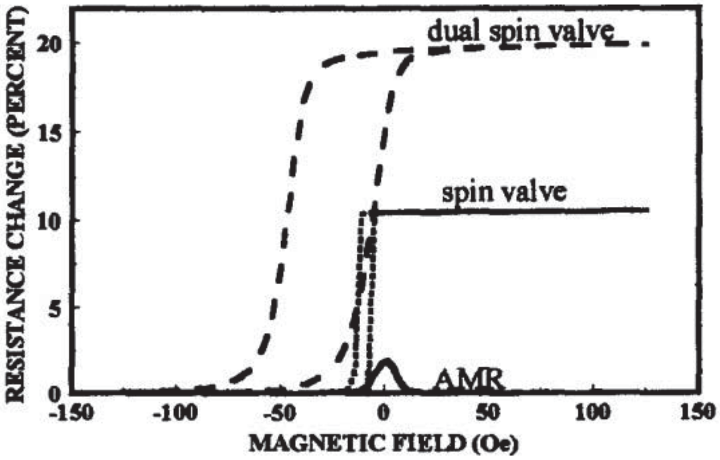

Figure I.4: Comparison of the percentage of resistance change for an AMR, spin vale and dual spin valve heads. [41].

have ratios closer to 2% in low fields and are very sensitive to crystallographic orientation. Giant MR was discovered to exhibit MR effects up to 50% change. This motivated researchers to study the magnetoresistive effects of coupling ferromagnetic layers with antiferromagnetic layers in the attempt to have more control over the magnetization without the necessity for stronger magnets [17]. Both AMR and GMR candidates make good materials for applications like read and write heads in disk drives due to the ability to change resistive states depending on the field orientation. The main difference from AMR is the GMR independence from the direction of the current flow. Because of the engineered design of the GMR application when a strong field is present the layers will overcome the antiferromagnetic coupling between them and ferromagnetically align causing an overall reduction in the resistance. This can produce a highly sensitive sensor for magnetic screening and is currently utilized in several medical applications. Without a field present, or a sufficiently low field, the layers are antiferromagnetically coupled and in an inherent high resistive state [3]. The last category refers to changes in resistance of 99.9% or more as can be seen in fig.I.5 [30]. This is still a relatively new classification, containing their own sets of questions. If the layers are instead built with

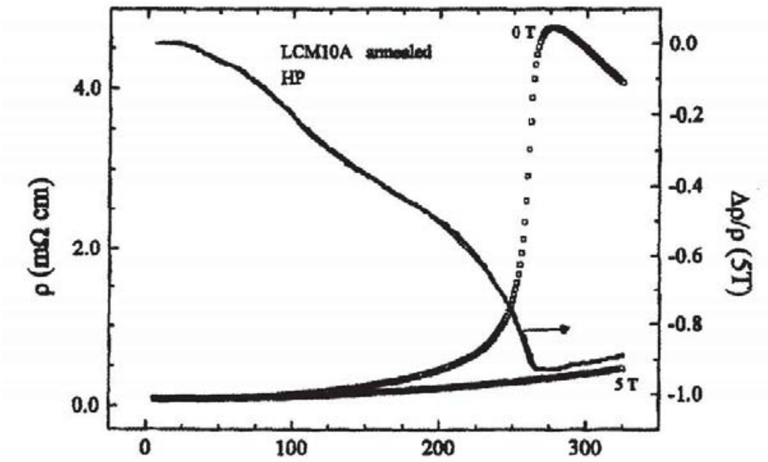

Figure I.5: CMR resistance in ambient field and 5 T. Note, at room temperature the changes is over 90% [41].

ferromagnetic materials separated by an insulating layer the material is said to be a tunneling MR (TMR) candidate. There does not seem to be any guidelines to categorize the change in resistance values for TMR and reports vary from 2.7% at room temperature [21] to 600% at room temperature with the change in resistance dramatically increasing at 4.2K with a change of 1100% [39]. An important distinction, though, should be noted. TMR is an effect created by appropriately designing a layered thin film system. The other classifications of magnetoresistance can hold true for bulk materials as well as thin films.

A significant problem still remaining with these materials is the field dependence of the resistance. Fields on the order of 10^4 Oe are required to obtain the large effect. Application of the field most likely increases the alignment of the spins, decreasing the resistivity. However, alternative mechanisms cannot be ruled out. For instance, the extremely large MR effect is only seen in epitaxially grown materials, with a much reduced effect in bulk materials. It has been shown that the lattice constant in the epitaxially grown materials is smaller than that in the bulk. Thus, it has been hypothesized that the distances between the magnetic ions is what is important, in that it will affect the indirect exchange interaction responsible for conductivity in these materials. Application of a magnetic field may affect the distances between the Mn ions, altering the frequency of the exchange coupling, and consequently the resistance [41].

I.B.2 Magnetocaloric effect

The magnetocaloric effect (MCE) is the reversible temperature change of a magnetic material upon the application or removal of a magnetic field [15]. Though some credit the discovery to Warburg in 1881 [59] and others credit Weiss and Piccard 36 years later [60], research laboratories have paired the magnetocaloric effect with cryogenic systems to achieve ultra low temperatures for decades in a process called adiabatic demagnetization [43]. However, as of April 2014 there is only one company manufacturing commercially available magnetic refrigeration systems (MRS). Cooltech Applications, according to their website, unveiled the first MRS in February 2014 at EuroShop, an international retail fair [11]. Magnetic refrigeration is a promising area for improvement as it is more energetically efficient than current processes which are based on the compression/expansion of gases. Magnetic refrigerator prototypes can achieve 60% of ideal (Carnot) efficiency, whereas the best commercial conventional refrigerator units can reach only 40% [15]. In addition Cooltech touts a reduction in electricity consumption of up to 50%. Moreover, as no refrigerant gases are required for magnetic refrigeration, there is no concern about ozone depletion or greenhouse effect, which contributes further to its environmental appeal [11].

I.C Superconductivity

Superconductivity was first observed by Kamerlingh Onnes in 1911 with the observation of a dramatic drop in the resistance of mercury metal below T_c = 4.15 K. The discovery rode the coattails of the first liquefaction of helium in 1908, also by Kamerlingh Onnes. He observed the resistance drop to zero below the critical temperature, T_c, making perfect conductivity a trademark characteristic of superconductivity. Another characteristic feature, below T_c superconductors exhibit perfect diamagnetism, as discovered by Meissner and Ochsenfeld in 1933. They found that not only was an applied magnetic field excluded from entering a superconductor (the case of a perfect conductor), but that an external field is also expelled as the material is cooled through T_c and transitions into its superconducting state. A superconductor can have persistent currents with or without an applied field. This phenomenon is called the Meissner-Ochsenfeld effect and implies that at some critical field, superconductivity will be destroyed. Empirically, this critical field, H_c(T) can be approximated by

$$H_c(T) \approx H_c(0)[1 - (\frac{T}{T_c})^2] \tag{I.6}$$

where $H_c(0)$ is the field at $T = 0$ K [56]. In 1957 Bardeen, Cooper, and Schrieffer (BCS) published a comprehensive theory of superconductivity providing a microscopic framework for the phenomenom. BCS theory states that any attractive interaction between electrons may lead to the formation of Cooper pairs. In conventional superconductors, the attraction is phonon mediated. The attractive potential is due to conduction electrons locally contracting the lattice, resulting in an area of greater positive charge density. Another electron, some distance away, is then attracted to this charge distortion (lattice vibration - phonon). This indirect attraction binds the electrons, forming Cooper pairs. Cooper pairs are defined as quasi-particles which follow Bose-Einstein statistics, allowing them to occupy a single quantum mechanical state. The formation of Cooper pairs results in a superconducting ground state and the formation of an energy gap (E_g) at the fermi level [26, 56, 58]. Systems that do not follow BCS theory and therefore need more elaborate explanations to describe the mechanisms of superconductivity are considered to be unconventional superconductors. A few systems where unconventional superconductivity is observed is in $CeCu_2Si_2$, $CePd_2Si_2$ UPt_3, $CeIn_3$, $CeCoIn_5$, and $CeIrIn_5$.

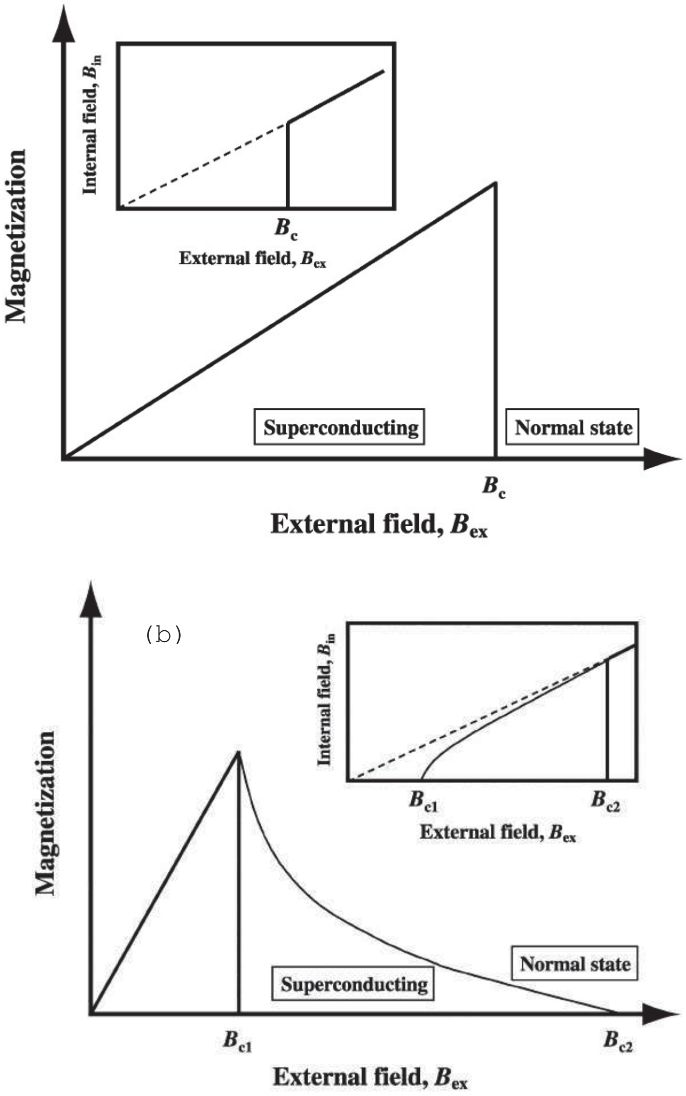

Figure I.6: (a) illustrates the magnetization, M, as a function of the applied magnetic field of a Type I superconductor. The inset shows the internal magnetic field strength B_{int}. (b) Magnetization, M, as a function of the applied magnetic field of a Type II superconductor. The inset shows the internal magnetic field strength B_{int}. [34]

There are two types of superconductors, Type I and Type II. Type I superconductors are characterized by having sharp transitions to the superconducting state and displays "perfect" diamagnetism up to a critical field H_c as displayed in fig. I.6. Type II superconductors are characterized by a transition to a superconducting state via a "mixed state" between to critical fields, H_{c1} and H_{c2}. At low fields, $H < H_{c1}$, Type II superconductors repel the applied magnetic field. Above H_{c1}, the material allows the magnetic field to penetrate in the form of magnetic flux lines up to a second critical field, H_{c2}, at which point the vortex cores overlap, bulk superconductivity is destroyed and the material returns to its normal state. Between H_{c1} and H_{c2}, the flux density is non-zero and the Meissner effect is said to be incomplete. The H_{c2} can be significantly larger than H_c of Type I superconductors. The largest H_c for Type 1 superconductors is approximately 0.1 T, whereas Type II superconductors can persist in fields up to 200 T [58].

I.D Fermi Liquid Behavior

Landau developed the Fermi Liquid (FL) theory as a phenomenological theory to describe normal metals at low temperatures. In the free electron model, electrons are treated as non-interacting. For $k_T \ll E_F$, where E_F is the Fermi energy, the physical properties of a non interacting gas are given by the following equations:

$$\frac{C(T)}{T} = \gamma_0 T = \frac{\pi^2 k_B^2}{3}(N(E_F)) \tag{I.7}$$

$$\chi(T) = \chi_0 = \mu_0 \mu_B N(E_F) \tag{I.8}$$

$$\rho_{el-el} \sim c(\frac{k_B T}{E_F})^2 \tag{I.9}$$

where $N(E_F)$ is the density of states at the Fermi energy, E_F, k_B is Boltzmann's constant, μ_0 is the permeability of free space, μ_B is the Bohr magneton, ρ_{el-el} is the resistivity due to electron-electron scattering, and c is the microscopic scattering cross section. However the free electron picture is not complete since it fails to describe many phenomena. The weak electron-electron and electron-phonon interactions results in deviations of the thermodynamic and transport properties (C(T)/T), χ(T), ρ(T)) at low temperatures. Landau's solution to this problem was to introduce an electron-like quasiparticle with a modified effective mass, m^*. Qualitatively, this kind of quasiparticle is an electron "dressed" with the interactions of other electrons in the system. If we assume the electron-like quasiparticle can have one to one mapping with a non-interacting electron gas, the FL model predicts that the low temperature properties will act as a free electron gas, but with an enhanced mass m^* and a few additional parameters. Landau successfully explains the free electron model despite the strength of electron - electron interactions and predicts the temperature dependence of the thermodynamic and transport properties according to these interactions. The FL picture of the specific heat, $C(T)/T$, the magnetic susceptibility, $\chi(T)$, and the resistivity, ρ, are give by the following equations:

$$\frac{C(T)}{T} = \gamma_0 \frac{m^*}{m_e} = \gamma \tag{I.10}$$

$$\chi(T) = (\frac{m^*}{m_e})(\frac{\chi_0}{(1+F_0^a)}) \tag{I.11}$$

$$\rho = \rho_0 + AT^2 \tag{I.12}$$

$$A \sim (\frac{k_B}{N(E_F)})^2 \tag{I.13}$$

where F_0^a is an additional Landau parameter, which takes into account residual interactions among the quasiparticles [2, 5, 26].

I.E Heavy Fermion Behavior

Heavy fermion (HF) systems are typically formed from $4f$ and $5f$ atoms, predominantly consist of Ce, Yb, and U systems. HF compounds generally show an enhanced linear electronic contribution, characterized by the Sommerfield coefficient, γ, in specific heat, $C(T)$ at low temperatures compared to normal metals, subsequently resulting in an effective mass orders of magnitude larger than the free electron mass [36]. In the free electron approximation γ is related to the effective

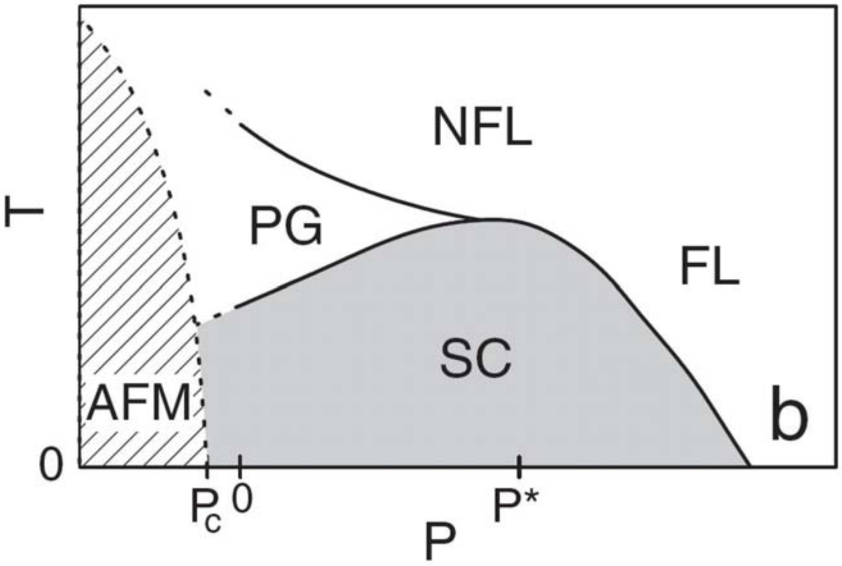

Figure I.7: Schematic phase diagram of CeCoIn5, where NFL is non fermi liquid behavior, SC is superconducting, FL is fermi liquid behavior, PG is pseudo gap state and AFM is the antiferromagnetic Neel state [50].

electron mass via:

$$\gamma = \frac{\pi^2 k_B^2 N(E_F)}{3} = \frac{k_B^2 k_F^2 m^*}{3\hbar} \tag{I.14}$$

where $N(E_F)$ is the Fermi energy level density of states, k_F is the Fermi wave vector, m* is effective mass of the electron. Simple metals typically obtain γ values on the order of 1-3 mJ/K^2 mol, resulting in m$^* \approx m_e$ (m_e is the free electron mass). For HF systems, the effective mass is determined from equation I.11 and is typically on order of $\sim 10^2$ - 10^3 m$_e$, thus the name “heavy” fermion.

HF systems are characterized as being in proximity to a magnetic instability which is due to the magnetic moment of the f ion and its hybridization with the surrounding conduction electrons. Experimentally, the strength of the hybridization can be tuned by chemical or hydrostatic pressure [52], since both affect the distance between the magnetic ions. Near the magnetic instability a variety of rich and exotic behavior develops, including long range magnetic ordering, the Kondo effect, and magnetically mediated superconductivity [37]. A classic example is the discovery of $CeCu_2Si_2$, by Steglich et al in 1979. It was the first HF Superconductor (HFSC) discovered with a $\gamma \approx 1100$ mJ/mol K^2 corresponding to an effective mass $m^* \sim 100$ m_e [53]. Despite a low superconducting transition of $T_c = 0.65$ K , it proved to be a prime candidate for complex order parameters and non-electron phonon mediated pairing. Since its initial discovery in 1979, over 30 HFSC have been identified [45].

I.E.1 Heavy Fermion Superconductivity

In the HF compounds, superconductivity almost always occurs at the border of magnetism. HFSC display a rich array of behavior and their superconductivity arises from the interactions of heavy quasiparticles. Conventional superconductivity is phonon mediated as described in section I.C. In addition the presence of magnetism, whether a magnetic field or magnetic moment, destroys superconductivity in the BCS picture of a conventional s-wave superconductor. However, there is possible evidence of magnetically mediated superconductivity in heavy fermion compounds. A physical picture implies that the presence of strong magnetic interactions between the $4f$ moments and the conduction electrons must overcome competing interactions, such that the magnetic interactions are responsible for the formation of cooper pairs [37]. The physical evidence is hard to observe due to narrow range of conditions in which it is predicted to occur.

I.F Kondo effect

In 1964 Jun Kondo [27] published a paper postulating the resistance minimum found in metal alloys with dilute paramagnetic impurities is due to the interactions between the spins of the conduction electrons and localized magnetic moments. Through the work of Kondo, Anderson, and Wilson the problem known as the Kondo effect can be described by the exchange Hamiltonian

$$H = -J s_c S_f \tag{I.15}$$

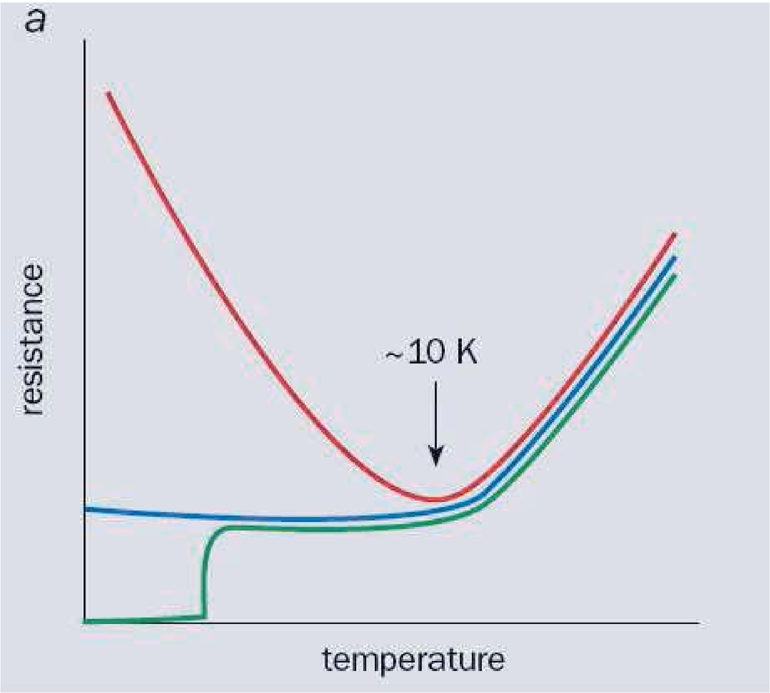

Figure I.8: As the temperature is lowered, the resistance of a normal metal decreases until it saturates to some residual value (blue line), otherwise known as the residual resistivity ρ_0. In the case of a superconductor (green line), the resistance abruptly goes to zero at a critical temperature T_c. However, in the case of the Kondo effect, where a small amount of impurities are introduced into a system, the resistance increases at low temperatures (red line) [28].

where J is the exchange constant, and S_f is the spin of the localized moment which interacts with the spins s_c of the conduction electrons [12]. An exchange process occurs between the spins of the conduction electron and the spin of the local moment, effectively flipping the spin of the conduction electron from spin up to spin down (or vice vera), simultaneously creating spin excitations in said conduction electrons. The scattering from the exchange creates an intermediate state and is macroscopically observed as screening of the impurity ion [28]. Experimentally, it is manifested as a $-lnT$ contribution to the electrical resistivity such that

$$\rho = \rho_0 + AT^2 - lnT + BT^5 \tag{I.16}$$

where ρ_0 is the residual resistivity, AT^2 is the Fermi liquid term as described in equation I.13., and BT^5 is due to lattice vibrations [27]. However, the Kondo term diverges as $T \rightarrow 0$ and approaches a characteristic temperature T_K (Kondo Temperature), derived by summing over the leading logarithmic terms [19] and is given by the following approximation:

$$T_K \propto T_F exp(1/N(E_F)|\mathscr{J}) \tag{I.17}$$

T$_F$ is the Fermi temperature, $N(E_F)$is the density of states at the Fermi energy, E_F, and $\mathscr{J}$ is the exchange interaction parameter. Experimentally this behavior can be seen when the magnetization falls below the free-ion moment value, $\chi < \chi_{exp,curie}$.

I.F.1 Kondo Effect in Heavy Fermion Systems

The Kondo effect described above generally characterizes the behavior of a Kondo impurity, where dilute amounts of $3d$, $4f$, or $5f$ impurities are dissolved into a nonmagnetic host such as gold (Au). The impurities are so dilute that the d or f orbitals do not overlap and the system does not order magnetically. It is possible to increase the number of impurities (ie. Ce, Yb, or U) such that the system begins to form a sublattice of these “Kondo effects”.

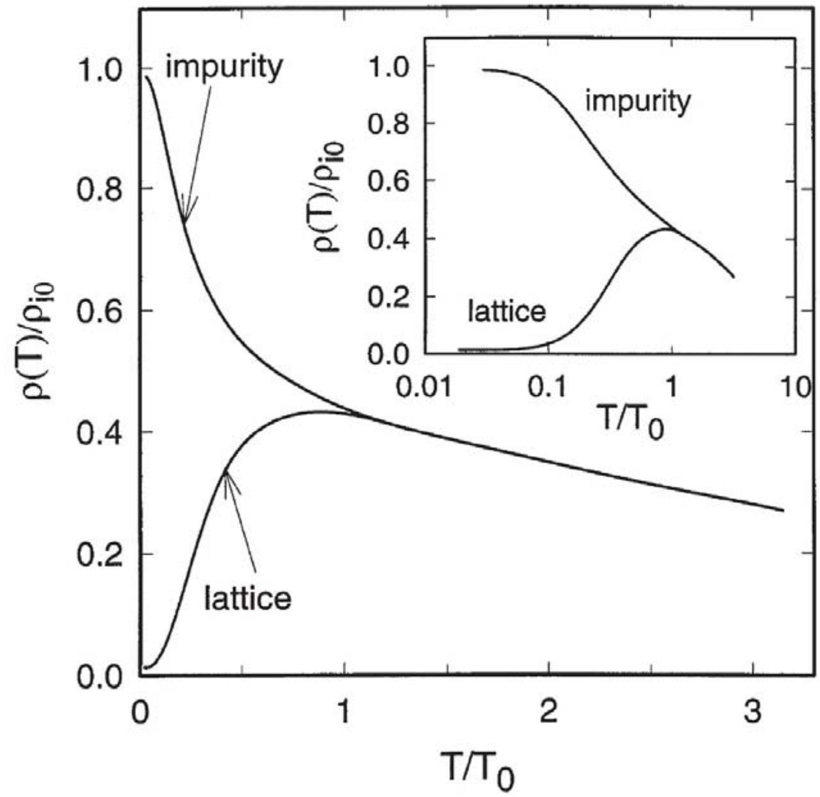

Figure I.9: Normalized resistivity $\rho(\mathrm{T})/\rho_0$ of the Kondo lattice with the lattice and the electronic contributions to resistivity as described in equation I.16[13].

A periodic array of the $4f$ or $5f$ magnetic moments is known as a Kondo lattice and has two major distinctions from the single ion Kondo impurity. First, the intersite interactions of the magnetic moments are no longer negligible, possibly giving rise to heavy fermion behavior. Second, as T decreases, magnetic impurities develop coherence due to the periodicity of $4f$ and $5f$ magnetic moments. At high T, the logarithmic term is negligible and as the system approaches some characteristic limit (T_{coh}), also known as the coherence temperature, the sublattice of magnetic moments is screened. Below T_{coh} Bloch states begin to form, resulting in a dramatic decrease in resistivity $\rho(T)$, where ρ typically behaves as a Fermi liquid in the lower temperature regime ($\rho = \rho_0 + AT^2$). A comparison of the Kondo impurity to the Kondo lattice in the temperature dependent resistivity ρ was calculated by Cox and Grewe (1988) [13] and is shown in fig.I.9. Their results are in good agreement with the observed experimental behavior. Examples of this crossover from incoherent scattering to strongly correlated Bloch states is seen in $CeCoIn_5$ [44], $CeCu_6$ [32], and $YbRh_2Si_2$ [57].

I.G Non-Fermi Liquid Behavior and Quantum Criticality

In 1991, Seaman et al. presented measurements on specific heat, electrical resistivity, and magnetic susceptibility on the system $Y_{1-x}U_xPd_3$ [48]. In the low temperature regime, $\rho(T)/\rho_0$ is almost linear in T and the specific heat $C(T)/T \sim -\ln(\alpha T)$. The results were intriguing because they firmly disagreed with the Landau Fermi Liquid model as described in section I.D. Since the initial observations of the anomalous low temperature physical properties, now known as non-Fermi liquid (NFL) behavior, many systems have been found. NFL behavior is observed in a variety of undoped systems at (or close to) a quantum critical point and has been induced by applying pressure, magnetic fields, or chemical substitution [54]. NFL behavior observed in resistivity, specific heat and magnetic

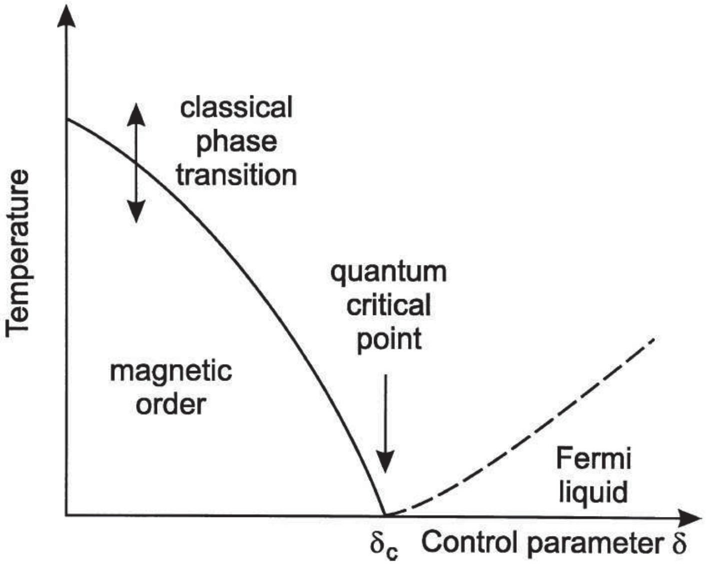

Figure I.10: ASchematic diagram of a magnetic instability driven by an order parameter, such as chemical substitution or pressure[33].

susceptibility measurements follow:

$$\rho \propto [1 - a(\frac{T}{T_0})^n] \tag{I.18}$$

$$\frac{C(T)}{T} \propto -\frac{1}{T_0} ln(\frac{T}{T_0}) \tag{I.19}$$

$$\chi(T) \propto [1 - (\frac{T}{T_0})^{1/2}] \sim -ln(\frac{T}{T_0}) \tag{I.20}$$

where $|a| \approx 1$ and $n \approx$ 1-1.5. The interest in NFL behavior has persisted for over 20 years because the origin of such behavior arises from several possibilities. In over 50 systems exhibiting NFL characteristics, the behavior may be due to magnetic instability leading to a quantum phase transition [33], multichannel Kondo effect [35], or a distribution of Kondo temperatures [6].

The interest in superconductivity near a quantum critical point is an area of great complexity and has been the subject of much experimental and theoretical work. The issue first arose in the wake of the high T_c cuprates when it became apparent that the origin of its superconductivity could not be explained by the phonon mediation. Quantum critical points are likely to occur at phase transitions close to absolute zero temperature when magnetic ordering has been suppressed by external means: pressure, magnetic field or chemical substitution. Phenomenologically, when a system approaches a second order phase transition as seen in fig.I.10, fluctuations of the order parameters slow down and occur over longer wavelengths. When a quasiparticle moves through a medium, it can generate large distortions which in turn can enhance the scattering cross section. This is limited by some sort of long range periodic magnetic ordering (typically antiferromagnetic) which can be viewed as frozen out fluctuations. In a first order phase transition of a system from a paramagnetic state to an ordered magnetic state, entropy should be zero when $T = 0$. This implies that a zero temperature phase transition should occur between two ordered states. As a system approaches a second order phase transition, the strong quantum spin fluctuations ultimately destroy the consistency of the Landau fermi liquid picture. This phase transition at $T = 0$ K is considered a quantum critical point because the quantum mechanics determines the fluctuations of the order parameter [47].

I.H Flux Growth Technique

Before describing the details of the research I would like to make one final note about the chosen method of synthesis for these mulitnaries. Traditional methods of preparing intermetallic materials tend towards three main processes: arc-melting, radio-frequency induction heating, and direct reaction of elemental components (termed solid state reactions). All three of these reactions involve high temperatures that often are difficult to obtain safely. There are also limitations to each of these methods.

When arc-melting a sample, for instance, a large amount of current is formed between the stinger and the water-chilled hearth, with the sample in between. The current will instantaneously melt the material into a boule while thermal contact with the water-cooled hearth quenches and freezes the microstructures that have nucleated within. This is a very nice and easy system to setup, however, this technique only works well for materials that do not form binaries at high temperatures and with materials of a sufficiently low vapor pressure. The amount of current can be controlled, but not to the extent of providing any measurable kinetic control. The structures that form within the boule are subject to the standard thermodynamic rules of phase nucleation. When arced, the metastable phases nucleate first and when the boule is quenched those phases will remain and the homogeneity of the sample may be improved through extended annealing. However, if the desire is an intermediate phase with a higher energy of formation than other phases than those desired phases are inaccessible by the arc-melting process. Radio-frequency induction heating has many of the obstacles as arc-melting since the process requires extremely high temperatures, but additionally requires more equipment, time and higher precision than arc-melting. Traditional solid state chemistry for direct reactions of elemental metals entails grinding and annealing powders repeatedly. Though this process is more conducive to annealing in lower temperatures, grinding the samples constantly is a very mechanically harsh process, but necessary in order to expose fresh surfaces on which the reactions occur. Researchers will often press reactant powders into pellets in order to achieve better theoretical densities of the individual grains. This is not a factor in products of flux growths since the product is a bulk crystal, ideally large and single domain/grain.

There is a difference in the way the atom bonds in an intermetallic compounds than in pure elemental metals. In elemental metals, the electrons are considered to be delocalized. Itinerant electrons are not necessarily homogeneously distributed, but nor are they randomly distributed or clustered. This implies that the atoms can transfer charge as needed. In intermetallics, however, the bonds are not generously distributed. The atomic bonds form with a slight ionic and/or covalent character and the electrons are more localized. This variance in atomic bonding is what creates the potpourri of characteristics, both physical and magnetic, that are highly interesting and material dependent. As a result of this material-driven variety, predicting which phases could become stable in a metallic melt is challenging and does not follow the same techniques (like electron counting or oxidation-number analysis) as do halides, oxides or chalcogenides. Because of the covalent bonding, the melting point of the solid is low. The low melting point is essential to the flux growth method, as will be discussed.

P. Jolibois is well known for being the first to grow nickel phosphides in a tin flux, as early as 1910 [31]. By submerging the components in liquid tin the melting points of the other constituents are lowered thereby allowing for reactions at much lower temperatures than needed for direct reaction of the material. Molten metal flux systems allow for an energetic system that can simultaneously dissolve material in one location and nucleate in another. The liquid solutions with impurities inside tend to form at lower melting temperatures due to stabilization energies lower than that of a pure material. At the instance of flux liquefaction the impurities stabilize the melt, decreasing the entropy and increasing the Gibbs free energy of the solution and thus the rate of diffusion. Kinetic control, the ability to control the thermal energy and hence the kinetic energy of the system, can be achieved to a reasonable degree by choosing appropriate annealing parameters. Rapid temperature transitions can lead to undesired phase formations, or microstructures, which will only increase in size and stability on the cooling trend so the idea is to avoid temperatures that encourage nucleation. However, the controlled state of the growth prevents rapid temperature transitions, allowing for phases that were not accessible before. Kanatzidis and his co-authors wrote the statement quite elegantly when they wrote, “The flux chemistry leads to the most feasible result under the prevailing conditions of reactant ratio and concentration. In other words, it ‘finds’ the accessible compositions regardless of complexity and this underscores the great potential of molten metals as reaction media for accessing novel multinary phases [24].” This allows for strange behavior like an atomic site being shared by two atoms of different metals since the decrease in the energy of formation leads to an increase in the rate of diffusion. To what extent a metal flux can allow this behavior depends upon the solubility of those starting ingredients in the molten metal.

Bibliography

[1] H. Aoki, T. Sakakibara, H. Shishido, R. Settai, Y. Onuki, P. Miranovic, and K. Machida, J Phys. Condens. Matter **16**, L13 (2004)

[2] N. W. Ashcroft, N. D. Mermin, Solid State Physics, (Brooks Cole 2000)

[3] M. Baibich, Phys. Rev. Lett. **61**, 2472 (1988)

[4] L. F. Bates, Proc. Roy. Soc. (London) **A117**, 680 (1928)

[5] E. Bauer, Encyclopedia of Materials: Science and Technology, 4181-4152 (2001)

[6] O. O. Bernal, D. E. Maclaughlin, H. G. Lukefahr, and B. Andraka, Phys. Rev. Lett **75**, 2023 (1995)

[7] A. J. Blattner, P. L. Prabhumirashi, V. P. Dravid and B. W. Wessels, Journal of Crystal Growth, **259** (1-2), 8-11 (2003)

[8] S. Blundell, Magnetism in Condensed Matter, Chap. 2, 7 (Oxford University Press, Oxford 2006)

[9] E. Bruck, O. Tegus, D.T. Cam Thanh, Nguyen T. Trung, K.H.J. Buschow, International Journal of Refrigeration **31**, 763770 (2008)

[10] C. Capan, G. Seyfarth, D.Hurt, B. Prevost, S. Roorda, A.D.Bianchi, and Z. Fisk, Europhys. Lett. **92**, 47004 (2010)

[11] http://www.cooltech-applications.com, accessed May 2014

[12] B. Coqblin, Encyclopedia of Materials: Science and Technology, 5018-5032 (2001)

[13] D. L. Cox and N. Grewe, Z. Phys. B **71**, 321 (1988)

[14] ”Fifty Years of X-Ray Diffraction, P.P. Ewald (Ed.), IUCr XVIII Congress (1962), Glasgow, Scotland; Online. April 24, 2014

[15] V. Franco, J. S. Blazquez, B. Ingale, and A. Conde, Annu. Rev. Mater. Res. **42**, 305-342 (2012)

[16] C. Guillaud, J. Phys. Radium **12**, 223 (1951)

[17] D. Heim, IEEE Trans. Mag. **30**, 316 (1994)

[18] F. Heusler, Z. angew. Chem. **1**, 260 (1904)

[19] A. C. Hewson, Phys. Rev. Lett. **70**, 4007-4010 (1993)

[20] S. Hilpert and T. Dieckmann, Ber. Deut. Chem. Ges. **44**, 2831, (1911).

[21] S. Ikeda, J. Hayakawa, Y. Ashizawa, Y.M. Lee, K. Miura, H. Hasegawa, M. Tsunoda, F. Matsukura and H. Ohno, Appl. Phys. Lett. **93** (i8), 082508 (2008).

[22] K. Izawa, H. Yamaguchi, Y. Matsuda, H. Shishido, R. Setta and Y. Onuki, Phys. Rev. Lett. **87**, 5 (2001)

[23] Y. M. Kalychack, V. I. Zaremba, V. M. Baranyak, V. A. Bruskov and P. Y. Zavalij, Izy. Acad. Nauk. SSSR Met **1**, 209 (1989)

[24] M. G. Kanatzidis, R. Pottgen and W. Jeitschko, Angew. Chem. Int. Ed. **44**, 6996-7023 (2005).

[25] J. S. Kim, J. Alwood, G. R. Stewart, J. L. Sarro and J. D. Thomspon, Phys. Rev. B **64**, 134524 (2001)

[26] C. Kittel, Introduction to Solid State Physics **8th edition**, 298-320 (2005)

[27] J. Kondo, Prog. Theor. Phys. **32**, 37 (1964)

[28] L. Kouwenhoven and L. Glazman, Physics World, 33-38 (Jan. 2001)

[29] A. Kwiatkowski, D. Wasik, P. Dluzewski, J. Borysiuk, M. Kaminska, A. Twardowski and J. Sadowski, J. Magn. Magn. Mater. **321**, 2788-2791 (2009)

[30] S. Jin, Science **264**, 413 (1994)

[31] P. Jolibois, C. R. Hebd, Seances Acad. Sci. **150**, 106-108 (1910).

[32] H. v. Lohneysen, Physica B **206-207**, 101-107 (1995)

[33] H. v. Lohneyson, Encyclopedia of Materials: Science and Technology, 6185-6191 (2001)

[34] P. Majewski, Encyclopedia of Materials: Science and Technology, 5018-5032 (2001)

[35] M. B. Maple, M. C. Andrade, J. Herrmann, Y. Dalichaouch, D. A. Gajewski, C. L. Seaman, R. Chau, R. Mosvshovich, M. C. Aronson and R. Osborn, J. Low Temp. Phys. **99**, 223 (1995)

[36] M. B. Maple, J. Phys. Soc. Jap. **74**, 222-238, (2005)

[37] N. D. Mathur, F. M. Grosche, S. R. Julian, I. R. Walker, D. M. Freye, R. K. W. Haselwimmer and G. G. Lonzarich, Nature **394**, 3943 (1998)

[38] T. R. McGuire, IEEE Trans. on Mag. **11:4**, 1048 (1975)

[39] T. Miyazaki and N. Tezuka, J. Magn. Magn. Mater. **139**, L231L234 (1995).

[40] F. C. Nascimiento, A. O. dos Santos, A. de Campos, S. Gama and L. P. Cardoso, Materials Research, Vol. **9**, No. 1, 111-114 (2006)

[41] J. Nickel, Magentoresistance Overview, CMR Workshop, Los Alamos National Laboratory, Feb. 9-10, 1995

[42] J. P. Paglione, M. A. Tanatar, D. G. Hawthorn, E. Boaknin, R. W. Hill, F. Ronning, M. Sutherland, L. Taillefer, C. Petrovic and P. C. Canfield, Phys. Rev. Lett**91**, 246405 (2003)

[43] V. Pecharsky and K. Gschneider Jr.,J. Magn. Magn. Mater. **200** 44-56 (1999)

[44] C. Petrovic, P. G. Pagliuso, M. F. Hundley, R. Movshovich, J. L. Sarrao, J. D. Thompson, Z. Fisk and P. Monthoux, J. Phys. Condensed Matter **13**, L337-L342 (2001)

[45] C. Pfleiderer, ArXiv Condensed Matter e-prints **arXiv:0905.2625v1**, (2005)

[46] L. Pytlik and A. Zieba, J. Magn. Magn. Mater. **51**, 199-210 (1985)

[47] A. J. Schofield, Contemporary Physics **40**, 95-115 (1999)

[48] C. L. Seaman, M. B. Maple, B. W. Lee, S. Ghamaty, M. S. Torikachvili, J. S. Kang, L. Z. Liu, J. W. Allen and D. L. Cox, Phys. Rev. Lett. **67**, 2882-2885 (1991)

[49] V. Sechovsky, Encyclopedia of Materials: Science and Technology, 5018-5032 (2001)

[50] V. A. Sidorov, M. Nicklas, P. G. Pagliuso, J. L. Sarrao, Y. Bang, A. V. Balatsky and J. D. Thompson, Phys. Rev. Lett. **89**, 15 (2002)

[51] A. Smits, H. Gerding, and F. VerMasst, Z. Physik. Chem. **357** (1931)

[52] F. Steglich and S. Sullow, Encyclopedia of Materials: Science and Technology, 3746-3750 (2001)

[53] F. Steglich, J. Arts, C. D. Bredl, W. Lieke, D. Meschede, W. Franz, H. Scafer, Phys. Rev. Lett. **43**, 1892 (1979)

[54] G. R. Stewart, Rev. Mod. Phys. **73**, 797-855 (2001)

[55] M. A. Tanatar , J. Paglione1 , S. Nakatsuji, D. G. Hawthorn1 , E. Boaknin, R. W. Hill1 , F. Ronning1 , M. Sutherland , Louis Taillefer, C. Petrovic P. C. Canfield, and Z. Fisk, Phys. Rev. Lett. **95**, 067002 (2005)

[56] M. Tinkham, Introductioon to Superconductivity, ch.1, (Dover, New York 1996)

[57] O. Trovarelli, C. Geibel and F. Steiglich, Physica B **284**, 1507-1508 (2000)

[58] R. Turton, Physics of Solids, ch.9, (Oxford Unviersity Press, Oxford 2000)

[59] E. Warburg, Ann. Phys. (Leipzig) **249**, 141-164 (1881)

[60] P. Weiss and A. Piccard, J. Phys. (Paris). 5th Ser. **7**, 103109 (1917)

[61] B. D. White, K. Huang, I. K. Lum, J. J. Hamlin, S. Jang, G. J. Smith, J. W. Simonson, C. S. Nelson, M. C. Aronson, and M. B. Maple, (submitted May 2014)

[62] B. T. M. Willis and H. P. Rooksby, Proc. Phys. Soc. (London) **B67**, 290 (1954)

[63] R. H. Wilson and J. S. Kasper, Acta. Cryst. **17**, 95 (1964)

II

Introduction to MnAs

With the advent of computers (and concepts such as designing and optimizing magnetic data storage) the need to understand magnetic properties of nanoscaled particles has increased and concepts like magnetoresistance and magnetocaloric effects have played large roles in motivating research [17, 20]. The renewed interest into magnetocaloric materials, i.e. magnetic refrigeration candidates, of which MnAs is a forefront material, is motivated by the ideal of replacing standard cryogenic refrigeration systems with magnetic refrigeration systems. Recent investigations are motivated by ongoing energy crisis and the acknowledgment of large, or colossal, magnetocaloric effect [6, 11, 19]. The purpose of this study was to investigate the nature of the bulk material in physical scales previously unobtainable.

MnAs was first reported at the turn of the 20th century by Heusler in 1904 [14], and can be thought of as a model for evolution of conceptual knowledge with advancing technologies. Original investigations by Heusler [14] and Hilpert and Dieckmann [15] were carried out on samples synthesized by direct elemental reaction and characterize the physical properties of the systems but not the magnetic properties. The discontinuous loss of ferromagnetism just above room temperature ($\sim$313K) became the subject of numerous studies over the next several decades [3, 4, 5, 12, 17, 23, 24, 27]. In the early sixties, there was speculation

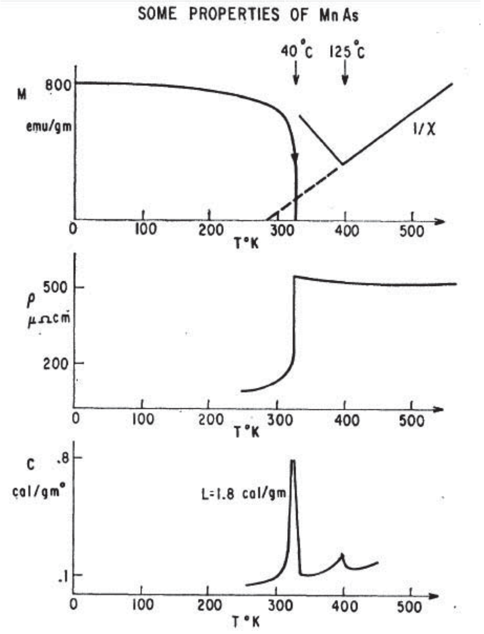

Figure II.1: Bean and Rodbell show some of the features associated with the first-order transition at 40°C as well as the second-order transition as measured at 120°C [4].

that this near-room temperature loss of ferromagnetism might be a first order transition, previously discounted since the entropy is continuous as it relates to the magnetization, and detailed measurements, as seen in fig. II.1 of specific heat, electrical resistivity and magnetization sought to confirm this suggestion [4]. Also, early reports concluded that although there was a deviation in a lattice parameter, affecting the volume density, there was no change in the crystal symmetries associated with the transition [12, 25]. This, too, was reexamined in the early sixties and the structural transformation from a hexagonal structural to an orthorhombic structure was detailed at length in a study by Wilson and Kasper in 1964 [26]. The revised conclusion is a direct result of increased reliability of chemical analysis techniques and accessible with x-ray diffractometers and the databases created as detailed in"Fifty Years of X-Ray Diffraction, edited by P.P. Ewald in 1962 [9]. Both transitions, magnetic and structural, will be described in detail within the MnAs experimental details chapter.

III

MnAs Experimental Details

III.A Sample Preparation of MnAs flux growth

The compounds in this thesis were synthesized via flux growth to produce high quality single crystals. The melting temperatures, suppliers and purities are listed in table V.A. Due to the toxicity of working with pure arsenic and arsenic oxide, the sublimation temperature of arsenic needs to be factored into the heating curve as well.

MnAs single crystals were synthesized in a molten metal flux. Mn powder and InAs were weighed in a 1:5 molar ratio with Sn pieces in the molar ratio of 1:89 Mn to Sn. InAs was chosen as the vehicle for safe arsenic distribution due to the safer nature of the binary during assembly and the ease of removal of excess indium. None of the constituents required special preparation excepting the manganese powder, which was kept in an oxygen-free environment until weight and assembly. Crystals were also synthesized with slightly different starting ratios and quantities in order to ascertain the degree of flexibility with the synthesis method. The samples are distinguished throughout as the standard, the bulk, and excess InAs. The “standard” batch is described above. The batch identified as “Bulk” maintained the same ratios as the standard but the total amount of material was increased threefold to identify an weaknesses in bulk synthesis. The “Excess InAs”

Table III.1: Melting temperatures, supplier, and purities of elements used in this thesis

Element	Melting Temp. (°C)	Supplier	Purities
Mn	1245	Alfa Aesar	99.9%
InAs	938	Alfa Aesar	99.9%
Sn	230	Alfa Aesar	99.9999%
In	160	–	–
As*	614 s.p.	–	–

batch contained excess InAs in the molar ratio of 1:10 Mn:As. These crystals were compared against each other as well as with the previously published data from MnAs in various forms.

It has been observed that certain elements, molten tin among them, can react with the quartz causing devitrification. The quartz is initially in a vitrified state, meaning a metastable, glassy state, of a tetragonal nature. Devitrification occurs upon atomic ordering and restructuring of the quartz into a stable cubic phase known as cristobalite, potentially causing the quartz ampoule to break during the process. The density of the quartz decreases and as a result the quartz turns opaque, if not completely white. In this study, fractures in the quartz are most likely occur during the structural change resulting in a decrease in density of the quartz. These fractures in the quartz are then exacerbated by either ongoing atomic changes in the cristobalite that can occur at both high and low temperatures or the pressure gradient normally required for successful synthesis; perhaps a combination of both [13]. To overcome these difficulties, the materials were layered into alumina crucibles with half the Sn on the bottom, the Mn powder sprinkled over the InAs pieces and the rest of the Sn on top. Ta foil (99.95%), 0.025 mm thick, covered the open end of the crucible instead of quartz wool and was secured with Ta wire, 0.025 mm in diameter. Five small holes in the foil was experimentally determined to be the most successful design for isolating the single crystals from the molten flux during centrifugation. The packed crucible was then placed in a quartz ampoule (14 in ID, and 16 in OD) and a mixed hydrogen/oxygen flame was used to shape the quartz into two chambers separated by a thin capillary approximately 1 inch above the crucible. Extra care was taken during the shaping process to avoid melting any constituents prematurely as this could result in arsenic exposure. The shaped quartz ampoule was placed on a vacuum line and evacuated down to 20 mtorr using a mechanical vacuum pump and refilled with argon gas five times to remove any oxidizing atmosphere. The alumina crucible was sealed in two layers of evacuated quartz to ensure the safety of both the sample and the lab.

Two ampoules were placed in the center of a Lindberg 1200○C box furnace, near the thermocouple so as to ensure the most accurate temperature measurement. The ampoules were heated slowly from room temperature to 1000°C over 10 hrs and allowed to dwell there for 48 hrs. Following a slow cooling to 650°C over a period of 48 hrs (-8.3°C per hour), the ampoule was centrifuged at 600°C to remove the molten flux metals, tin and indium, without the formation of undesired phases that are energetically more stable at lower temperatures, shown in the phase diagrams in fig. IV.2. The temperatures used in the heat treatment were determined from binary and ternary phase diagrams accessed online through ASM International's Alloy Phase Diagrams Center [2].

Once cooled the as-grown single crystals were encompassed by a combination of indium and tin. After investigations into the chemical hardiness of the samples, a chemical procedure of alternative chemical etches were employed. First, the as-grown crystals and any soft metal were gently mechanically removed from the crucible so as to minimize exposure time to the acidic treatment. With the bulk of the soft metals removed, the crystals were etched in dilute solutions of HCl (by volume: 1 part HCl to 4 parts DI H_2O) to remove any residual Sn on their surfaces. This was followed by a short exposure to dilute mixed solutions of HCl and HNO_3 (by volume: 14.5 parts HCl to 1 part HNO_3 to 80.5 parts Di H_2O). The crystals were thoroughly rinsed and visually inspected after each treatment to ensure no microscopic defects formed during the treatment. The most abrasive part of the

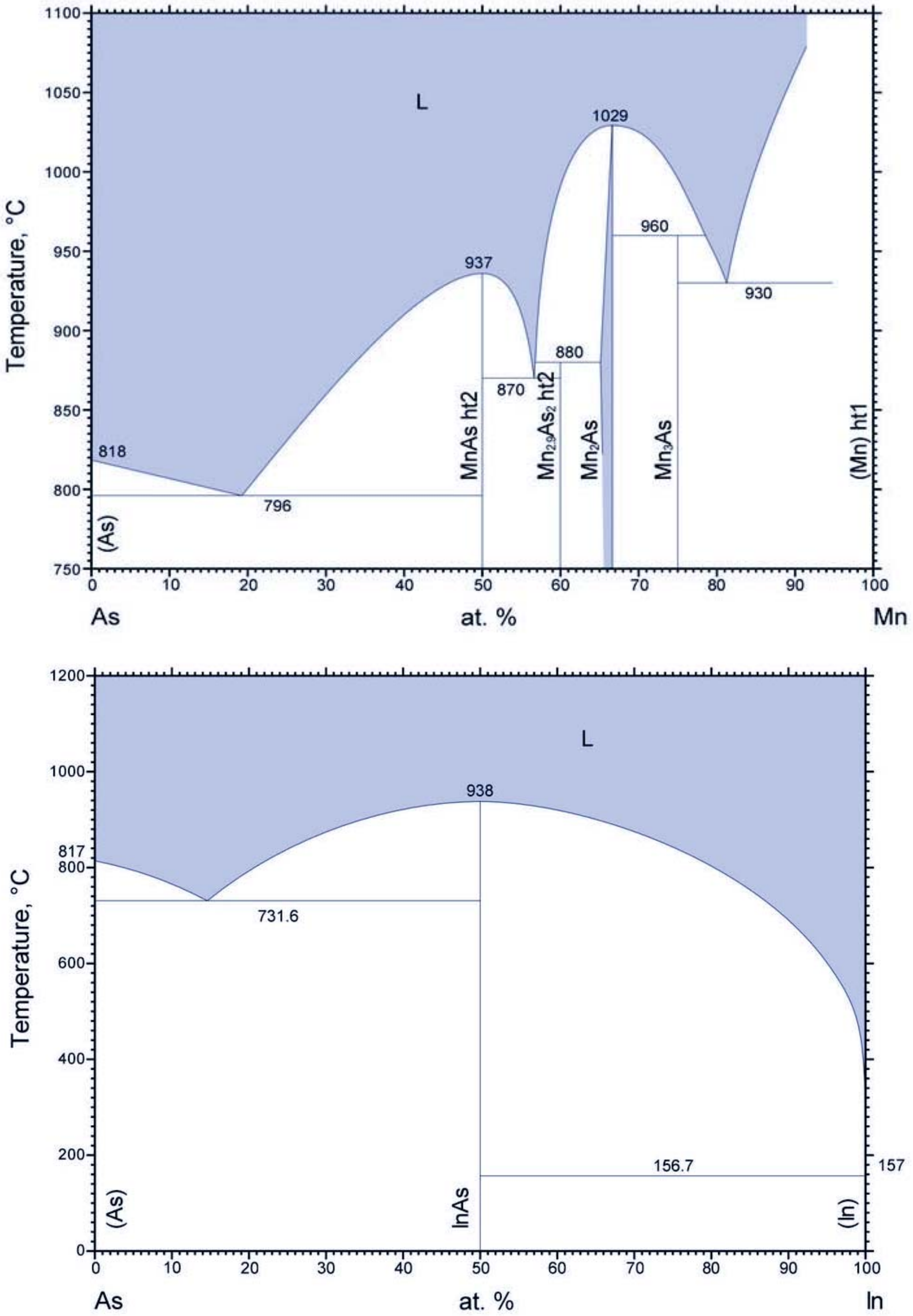

Figure III.1: Phase diagram of (a) Mn - As [21]and (b) In - As [1].

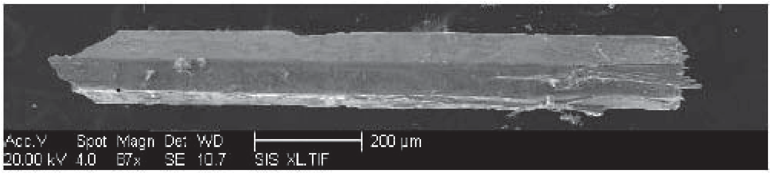

Figure III.2: A single MnAs crystal grown in the molten metal flux and its dimensions; picture taken under a scanning tunneling electron microscope.

process is the mechanical removal of the flux metals as the crystals are brittle with a small cross-sectional area and therefore break easily. However, the single crystals obtained by this method are relatively clean and undamaged as well as resistant to chemical exposure. The major advantages over previously reported MnAs single crystals are the ease of accessibility to specimens and the larger nature of the flux-grown samples. For example, there is no need to cut a single crystal from a large boule as in the other techniques such as the Bridgman technique employed by de Campos and his coworkers [8] nor are nano-facilities required to investigate these samples [7]. A representative crystal grown from the molten metal flux is shown in figure V.2 as capture by a scanning tunneling electron microscope.

III.B Characterization

As previously reported, MnAs has a first-order magnetic transition from ferromagnetic ordering to a paramagnetic state near 317 K. This magnetic transition is accompanied by a crystallographic transformation from hexagonal structure to orthorhombic structure as well as a discontinuous volume expansion of approximately 2% [26]. In powdered samples there is a moment of $3.4\mu_B$ in the room temperature hexagonal phase. This first-order transition shows a large thermal hysteresis of approximately 7 K seen in fig. III.3. In the MnAs compound, a reverse transformation of second order from the MnP-type to the NiAs-type structure occurs at 398 K [6].

In the absence of a magnetic field, MnAs exhibits the following phases.

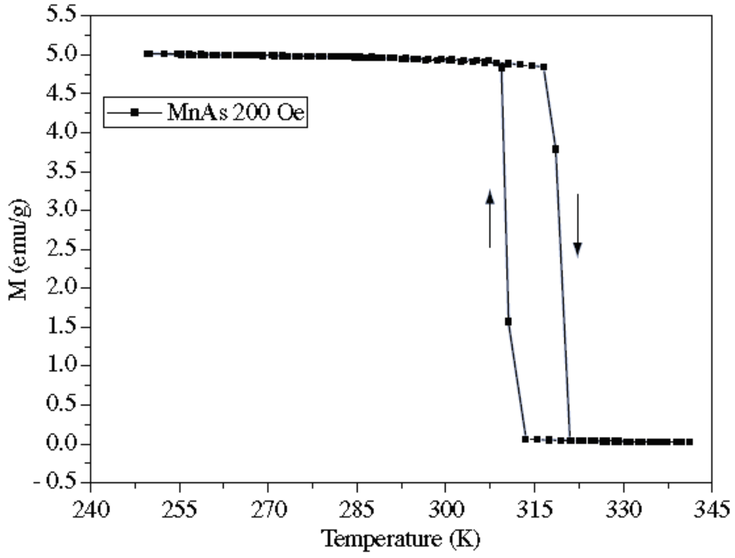

Figure III.3: Magnetization and thermal hysteresis under low applied field [19].

At high temperatures the crystal structure is hexagonal (NiAs-type) and paramagnetic. On cooling through $T_D \sim 394$ K, a second order transition to an orthorhombic structure (MnP type) takes place, but the material remains paramagnetic. When the material is cooled further through $T_{C(1)} \sim 306$ K, a first order transition from the paramagnetic phase to a ferromagnetic phase takes place, and as can be seen in fig. III.6, the crystal structure changes back to the NiAs type. This para- to ferro- transition shows hysteresis, and is observed at a higher Curie temperature, $T_{c(2)} \sim 317$ K, when the material is warmed. It is clear from fig. III.5 that at $H_0 = 0$ the MnP-type phase is confined to the temperature interval between the Curie point [$T_{c(1)}$ or $T_{c(2)}$] and T_D [28].

III.B.1 X-ray Diffraction

Thin hexagonal shaped crystals were collected and etched in hydrochloric acid to remove excess In and Sn flux from the surface. To verify the structural character and composition of each synthesis, several single crystals were collected and ground using an agate mortar and pestle. A clean glass slide was chosen and three layers of scotch tape was wrapped around the short length of the slide, such

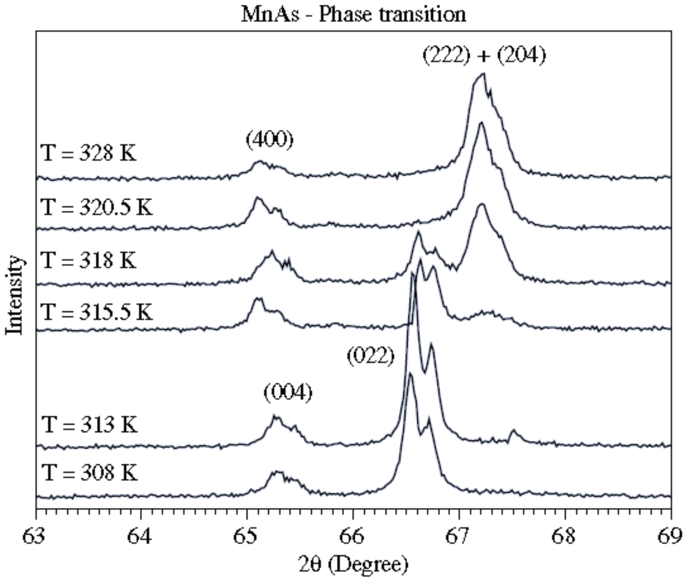

Figure III.4: Evolution of structure from orthorhombic to hexagonal when cooled through the first-order transition [19].

that there were two sets of three tape layers with approximately 3 mm between the tape. The tape layers were used to ensure an even thickness of powder. The powder was mixed with petrolatum jelly to form an opaque paste and then smeared between the two taped layers on the prepared glass slide. Another clean glass slide was used to smooth the surface of the paste. The tape was removed before any measurements were taken. X-ray powder diffraction measurements were completed on a commercial Bruker AXS Discover D8 X-Ray diffractometer at room temperature with a fan circulating vapor from a container filled with liquid nitrogen. The intent was to minimize potential phase transformation due to temperature creep within the measurement chamber. The powdered x-ray diffraction slides were then warmed on a hot plate and scanned again to achieve the orthorhombic phase. The intensity was measured as a function of 2θ from 20° - 95° using Cu $K_1\alpha$ radiation.

Several crystals were measured from each batch. The published literature for powdered samples and thin films report lattice parameters for the hexagonal $P6_3/mmc$ of 3.724 Å and 5.706 Å for a and c, respectively, at room temperature,

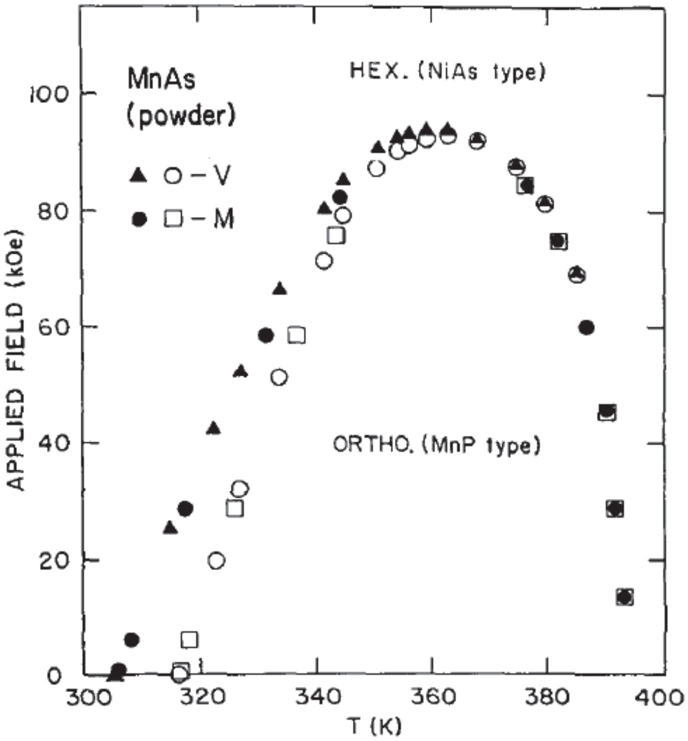

Figure III.5: Experimental phase diagram for magnetization and volume. Filled data points correspond to structural transitions from orthorhombic to hexagonal. Unfilled data points are transitions from hexagonal to orthorhombic [28].

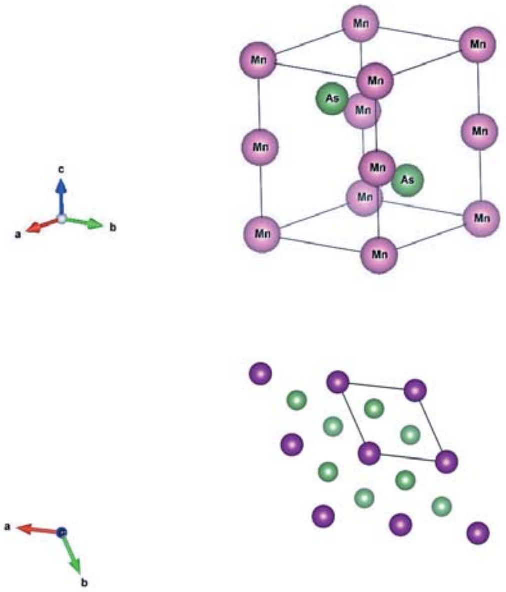

Figure III.6: Single crystals were ground and measured in the hexagonal $P6_3/mmc$ structure before structural phase transformation. The top picture illustrates the unit cell while the middle picture highlights the hexagonal structure.

20° C [25]. The orthorhombic $Pnma$ parameters are reported as 5.72 Å for a, 3.676 Å for b and 6.379 Å for c at temperatures starting just above 40° C[26]. As can be seen in table III.B.1 the crystals produced in this study are all in good agreement with the reported values for both structures. At room temperature, the lattice parameters deviate less than 1% amongst the batches themselves.

Samples were subsequently sent to the National Synchrotron Light Source (NSLS) to measure the evolution of the lattice and crystal structure as a function of temperature. In Fig. III.7, the hexagonal lattice parameters a_{hex} and c_{hex} are plotted as a function of temperature for $T < T_C$ and the orthorhombic lattice parameters a_{orth}, b_{orth}, and c_{orth} are plotted for $T > T_C$ [27]. The plots follow the relations laid out by Wilson and Kasper describing the relationship between the hexagonal and orthorhombic unit cells via the transformation: $a_{orth} = c_{hex}$, $b_{orth} = a_{hex}$, and $c_{orth} = \sqrt{3}a_{hex}$ [26].

In previous XRD measurements of polycrystalline samples, the thermal

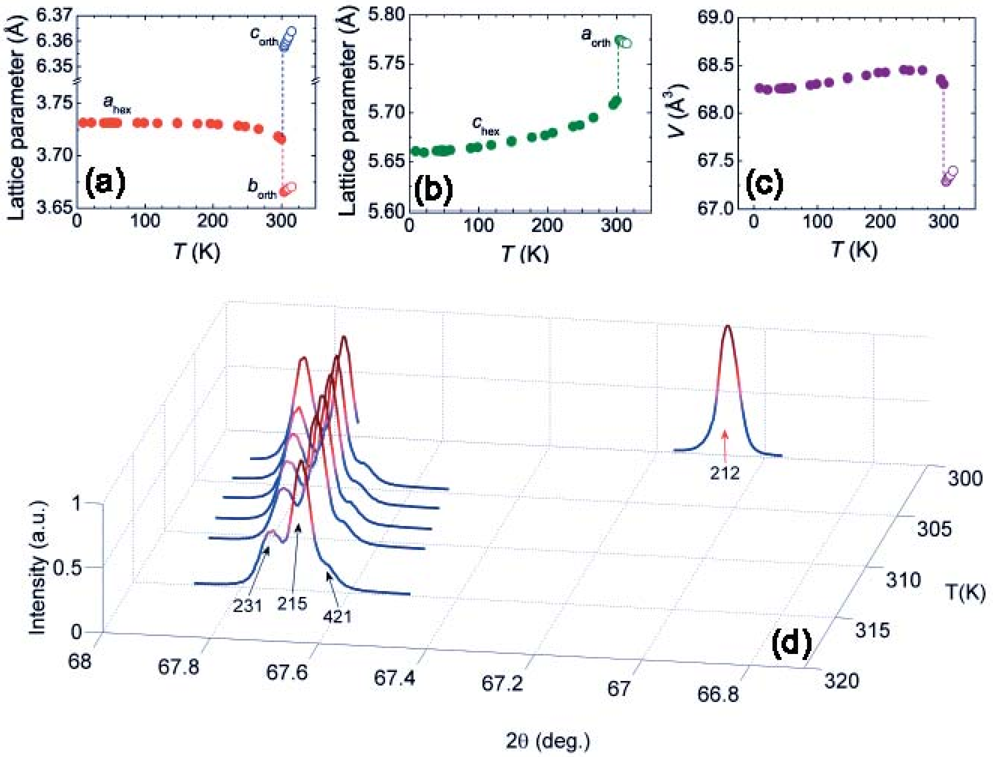

Figure III.7: The temperature dependence of the structural transition was investigated at the National Synchrotron Light Source. The dashed lines indicate a discontinuous jump at T_C; (a) the evolution of a_{hex} when $T < T_C$(filled circles) to b_{orth} and c_{orth} when $T > T_C$(unfilled circles); (b) the evolution of c_{hex} for $T < T_C$ (filled circles) to a_{orth} when $T > T_C$ (unfilled circles); (c) the volume transformation surrounding T_C; (d) The hexagonal [212] Bragg reflection, which vanishes at T_C, is shown at a temperature (corresponds to the right scale) near T_C. The orthorhombic [231], [215], and [421] Bragg reflections emerge for $T > T_C$ and their evolution with T is shown as a function of 2θ [27].

Table III.2: Lattice parameters of the various syntheses as compared to published standards.

Sample	a(Å)	b (Å)	c (Å)
Hexagonal $P6_3/mmc$			
powder [25]	3.724	3.724	5.706
Standard	3.715112	3.715112	5.699037
Bulk	3.721781	3.721781	5.713622
Excess InAs	3.718014	3.718014	5.71280
Orthorhombic $Pnma$			
powder [26]	5.720	3.676	6.379
Standard	5.771692	3.648057	6.361968
Bulk	5.718965	3.679898	6.389789
Excess InAs	5.724716	3.666082	6.396707

expansion has been shown to be quite anisotropic [25]. A large, discontinuous volume change in MnAs was observed at T_C, which occurs completely within the basal plane (a_{hex} is ∼0.93% larger than b_{orth} at T_C). On the other hand, thermal expansion perpendicular to the basal plane is reported to be continuous across T_C [25]. The thermal expansion we measured for our single crystals within the basal plane and perpendicular to the basal plane, respectively, is shown in Figs. III.7(a) and III.7(b). The discontinuous jump in the basal plane at T_C, calculated to be ∼1.34% by comparing a_{hex} and b_{orth} values at T_C (see Fig.III.7(a)), is larger than the previously reported value from polycrystalline samples. Another more significant difference is that there is a ∼1.09% increase at T_C between c_{hex} and a_{orth} (see Fig. III.7(b)), despite the previous reports of a continuous thermal expansion across T_C perpendicular to the basal plane. It is also notable that negative thermal expansion is observed in the orthorhombic phase of our single crystals ($T_C \leq T < T_S$) perpendicular to the hexagonal basal plane (see a_{orth} in Fig. III.7(b)). The hexagonal unit cell volume, V , calculated from our measurements of the lattice parameters, is plotted in Fig.III.7(c)for $T < T_C$, and half the orthorhombic unit cell volume is plotted for $T > T_C$. This choice was made because the volume of the orthorhombic unit cell is, by definition, exactly twice that of the hexagonal unit cell [26]. The plot of volume in Fig. III.7(c), therefore, displays the intrinsic

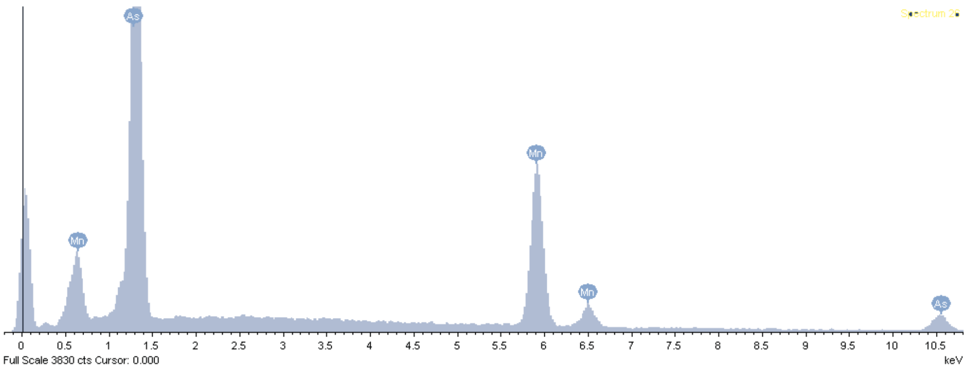

Figure III.8: EDS measurements were performed on several single crystals from each batch. The intensities of the elemental excitations are in arbitrary units and can be similar to other elemental standards. The results were well in accordance with one another suggesting consistency with the synthesis methodology.

discontinuity at T_C in the volumetric thermal expansion. Upon warming through T_C, the volume of our MnAs single crystals decreases by ∼1.5%, which is less than the previously reported value of ∼1.86%. This discrepancy is related to the fact that, while there is a larger decrease in the basal plane dimensions at T_C, it is counterbalanced by an increase in the dimension perpendicular to the basal plane. The XRD measurements were performed to a maximum temperature of 315 K, so the behavior of our single crystals in the vicinity of T_S was not studied. Previous reports of such measurements show subtle inflections in the temperature dependence of the lattice parameters at T_S [25]. In Fig. III.7(d), the hexagonal [212] Bragg reflection is shown at a temperature (corresponds to right-hand axis) near T_C. For $T > T_C$, this peak is absent and the evolution of the orthorhombic [231], [215], and [421] Bragg reflections with temperature is shown as a function of 2θ. Based on the work of Wilson and Kasper, at T_S (not measured), these Bragg reflections are expected to vanish and the [212] hexagonal peak will re-emerge [26].

To verify chemical composition and homogeneity amongst batches several single crystals were measured by energy dispersive spectroscopy (EDS). EDS is an analytical technique used for elemental or chemical characterization, relying on the atomic interactions between the x-ray source and the material. It relies on the principle that every element has a unique structure and therefore a corresponding excitation specific to a given wavelength. When an electron is excited out of its shell an electron hole is created. An electron from a higher energy band then fills the hole and the difference in the energies may be released in the form of an x-ray. The number and energy of x-rays emitted are measured in EDS scans. A more in depth explanation into the measurement is put forth in the third chapter. Prior to measurement, the crystals were visually inspected under a high resolution microscope for surface defects or contaminants. Once the surfaces of the crystals were determined to be sufficiently clean, some samples were strategically processed to expose different surfaces and cross sections. For example, a single crystal was well polished on one facet then broken into thirds. The first end was kept in its lightly polished state, the other end of the crystal was sanded and polished until the surface exposed was roughly halfway through the original crystal and the middle was mounted upright on the adhesive so the interior, *ab*-plane, was exposed and mostly unprocessed. Most of the crystals were mounted with the c axis parallel to aluminum mount by means of an adhesive and kept in a cool environment until the time of the measurement. Crystals without any exposure to acidic treatment were also measured to study the effects of the chemical etches.

The results shown in Fig. V.5 were consistent through the entire series suggesting that the variances employed during the assembly are fairly robust. The batch with excess arsenic was determined to produce crystals with quantities of arsenic comparable to the other synthesis ratios. This is consistent with the powdered x-ray results that showed an excess of InAs leftover when compared to the standard.

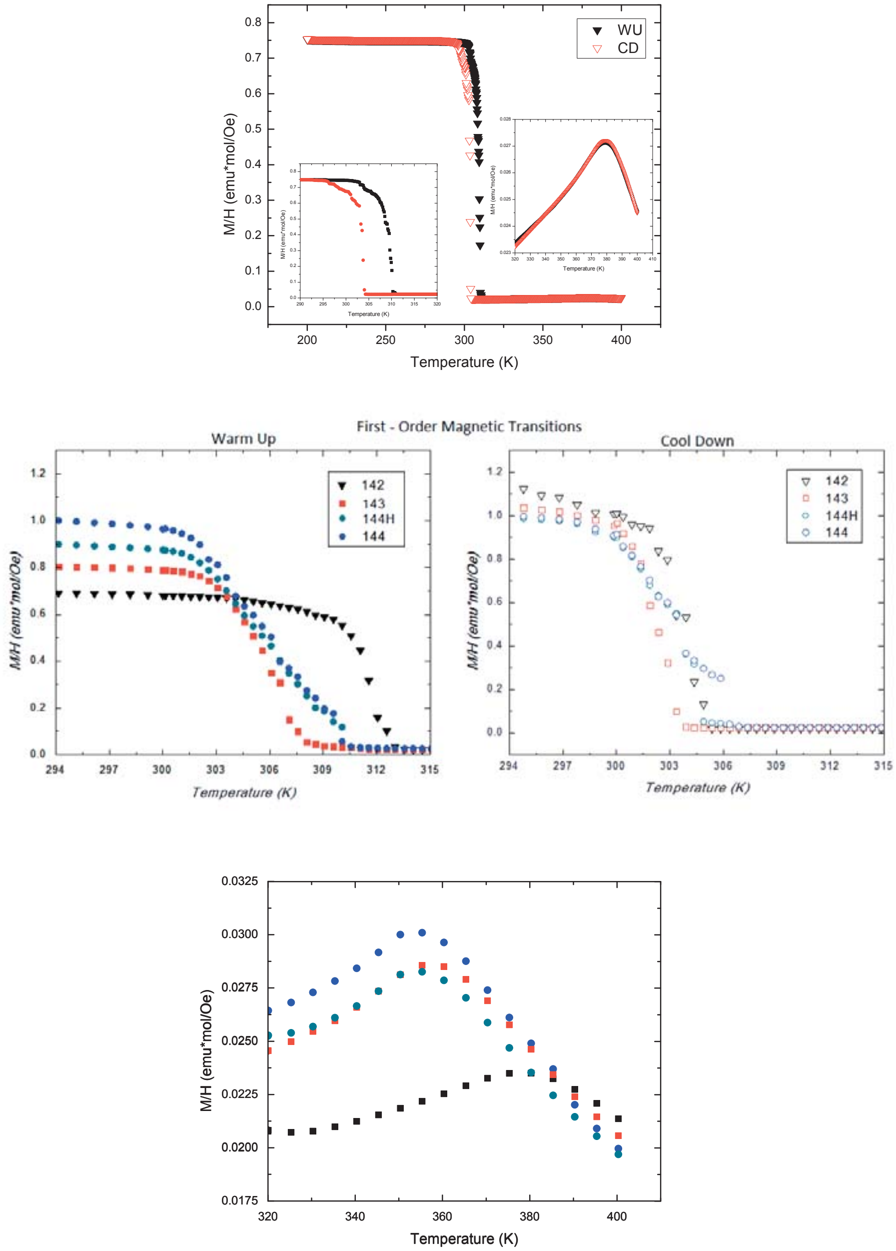

Figure III.9: (top) Magnetization overview of a single crystal;(middle) First order transition at roughly 302 K upon warming (306 K cooling), giving a hysteresis of 4 K. (bottom) The second order transition is observed near 355 K, occurs lower than the reported values [8, 25].

III.B.2 Magnetization

Magnetization measurements $M(H,T)$ were performed in a Quantum Design (MPMS XL-7) Superconducting Quantum Interference Device (SQUID) magnetometer and verified with a Quantum Design MPMS3. To prepare for such measurements on the MPMS XL an etched single crystal face was placed on 3M 1/4 in Kapton tape with the length of the crystal, the *c*-axis, parallel to the applied field direction, H $\parallel$ c axis. The sample was secured with another piece of Kapton tape and pulled through the length of a standard clear straw. For measurements in the MPMS3 the samples were mounted nonmagnetic sample mount affixed in the center with GE varnish. The mass of a single crystal used in these measurements was typically 1 mg. In both cases, the single crystal was at the approximate center of the sample mount, roughly 35 mm from the bottom of the sample probe. $M(T)$ measurements were measured from 10 K - 400 K under zero field cooled and field (1000 Oe) cooled conditions. Looking at the onsets of the ordering transitions, the first order transition temperature, on average, is 306 K upon warming and 302 K when cooling the sample. As can be seen in Fig. III.9, the onset of the first-order transition is lower than commonly reported in thin film samples, 315 K and 305 K for warming and cooling trends, respectively. This is also true of the second order transition. Many studies report values ranging from 380 K to just above 400 K [8, 27]. We see a fairly consistent transition around 355 K when the crystal returns back to its hexagonal state.

III.B.3 Resistivity

Samples for resistivity measurements, $\rho(T)$, were prepared using the standard four-wire technique. Crystals that were structurally similar in shape and size to the crystal shown in figure V.2 were chosen for this measurement. It was common to re-etch and polish the crystal to ensure there was no excess residue on the surface. After etching, the samples were secured to a glass slide by means of double sided tape while thin strips of aluminum foil were placed on the surface

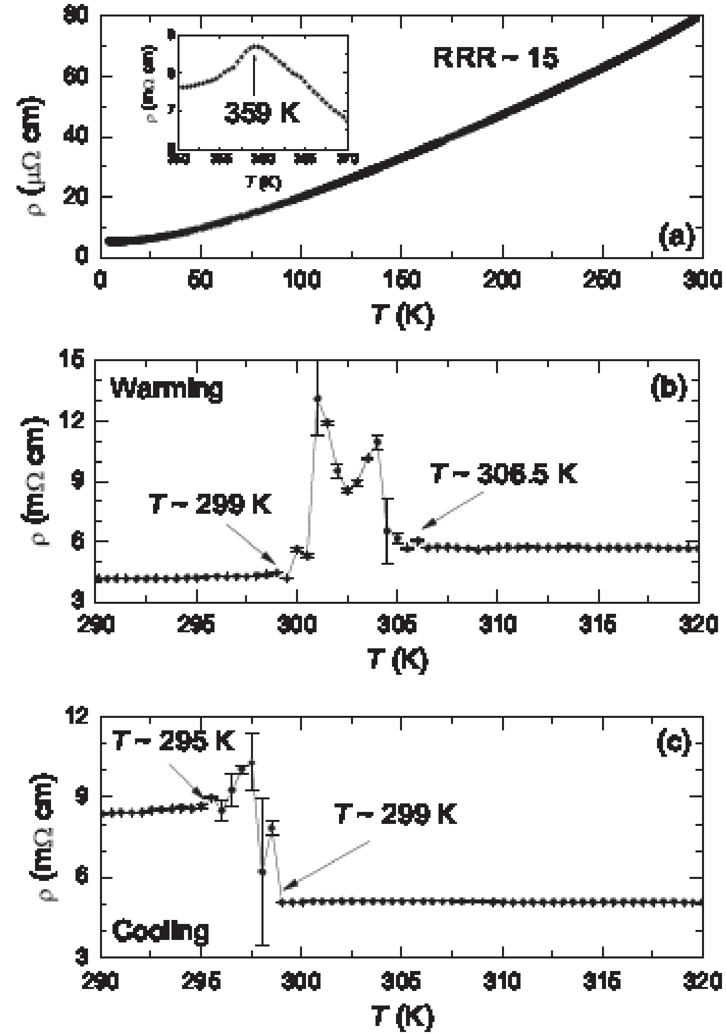

Figure III.10: Single crystals were prepared with the four wire lead configuration. The onsets of the first order transition, ∼299 K, are slightly lower than the onsets in the magnetization data, ∼303 K.

masking parts of the surface. The samples were sputtered with gold atoms using a Hummer 6.2 by Anatech LTD. operating for 15 - 20 minutes under ∼80 mtorr, at 15 mA and 6.5 kV. Once the foil is removed, four 1 mm gold wires were attached to the four gold contact pads of the sample with two-part silver epoxy Epotek-H20E, such that the leads were evenly spaced across the face of the single crystal. To cure the epoxy, the sample was placed in a Thermolyne low temperature box furnace at 200 °C for 5 min. Samples were measured in a Quantum Design PPMS DynaCool. Typical excitation currents applied to materials ranged from $1 - 10$ mA applied in-plane for a temperature range of 5.0 K - 380 K.

As can be seen in Fig. III.10 (a), the residual resistivity ratio was calculated to be approximately 15. The changes in resistances are at temperatures consistent with the rest of our measurements for a magnetostructural first order transition around 299 K and 306 K for warming and cooling trends respectively. Also, the change in the resistance at elevated temperatures, 359 K corresponding to the structural second order transition, is well supported by the magnetization results. The data points seen in the figures III.10 (b) and (c) are averages for approximately 30 single crystals with the error bars accounting for the standard deviation from these transition temperatures. There is evidence in the magnetization data that these single crystals might retain a memory and as such, processes such as thermal cycling, will cause irreparable damage to the crystal. The irreversibility is a great limitation and confirmation of behavior necessarily requires multiple samples to be measured. While the benefit is an inherent homogeneity check for each batch of material this difficulty does make it challenging to compare results with polycrystalline or thin film results. Based off the changes in the average resistance values, the bulk material still can be considered a candidate in the CMR based off the ratio of the change in resistance through the first order transition.

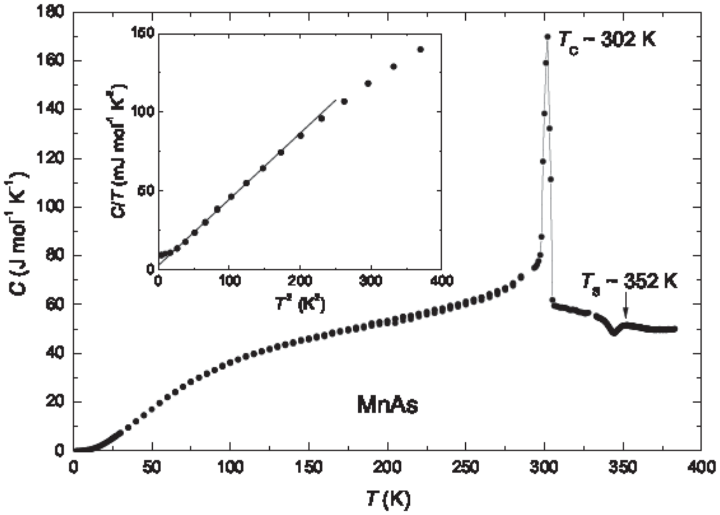

Figure III.11: Specific Heat C vs. Temperature T for MnAs. A sharp feature is observed at $T_C \simeq 302$ K, which is associated with the first order magnetostructural transition. A smaller feature, observed near $T_S \simeq 352$ K, is associated with the second order structural transition. The inset, C/T vs. T^2 is plotted and a line serves as guide for the fit $C(T)/T \simeq \gamma + \beta$ T^2.

III.B.4 Heat Capacity

Heat capacity measurements, seen in figure III.11 were carried out in a Quantum Design DynaCool utilizing their Heat Capacity Option software. The first order magnetostructural phase transition appears as a prominent feature near $T_C = 302$ K and a smaller feature associated with the second order structural phase transition is observed near $T_S = 352$ K, though this second order transition temperature seems to be sample dependent. Additionally, due to the inherent nature of the measurement, a single crystal cannot be scanned more than once without causing strains and deformation which will fundamentally change its behaviors. However, both of these transition temperatures are consistent with the T_C and T_S values observed in measurements of $M(T)$ and $\rho(T)$. The character of $C(T)$ is similar to an earlier report of measurements on a polycrystalline sample performed from low temperature to temperatures in excess of 400 K. The inset of Fig. III.11 displays C/T data vs. T^2. A linear fit between 4 K - 14 K of the expression $C(T)/T \simeq \gamma{+}\beta T^2$ to this data results in a Sommerfeld coefficient of γ = 3.2(3) mJ mol^{-1} K^2. This value of γ is smaller than the γ = 7.97 mJ mol^{-1} K^2 previously reported for a polycrystalline sample [8].

Bibliography

[1] I. Ansara, Colinet C. Chatillon, H. L. Lukas, T. Nishizawa, H. Ohtani, K. Ishida, M. Hillert, B. Sundman, B.B. Argent, A. Watson, T. G. Chart, and T. A. Anderson, Comput. Coupling Phase Diagrams Thermochem., Vol. **18** 1777-222 (1994)

[2] ASM Alloy Phase diagrams Center, P. Villars, editor-in-chief; H. Okamoto and K. Cenzual, section editors; ASM International, Materials Park, OH, USA, (2006-2013)

[3] L. F. Bates, Proc. Roy. Soc. (London) **A117**, 680 (1928)

[4] C. P. Bean and D. S. Rodbell, Phys. Rev. **126**, 104 (1962)

[5] A. J. Blattner, P. L. Prabhumirashi, V. P. Dravid and B. W. Wessels, JCG **259** (1-2), 8-11 (2003)

[6] Bruck O. Tegus, D.T. Cam Thanh, Nguyen T. Trung and K.H.J. Buschow, International Journal of Refrigeration **31**, 763 770 (2008)

[7] L. Dweritz, Reports on Progress in Physics **69**,2581-2629 (2006)

[8] A. de Campos, M.A. Mota, S. Gama, A.A. Coelho, B.D. White, M.S. Da Luz and J.J. Neumeier, JCG **333**, 54-58 (2011)

[9] “Fifty Years of X-Ray Diffraction, P.P. Ewald (Ed.), IUCr XVIII Congress (1962), Glasgow, Scotland; Online. April 24, 2014

[10] H. Fjellvg, H. D. Hochheimer, and W. Hnle, Phys. Lett. A **118**, 293-296 (1986)

[11] V. Franco, J. S. Blazquez, B. Ingale, and A. Conde, Annu. Rev. Mater. Res. **42**, 305-342 (2012)

[12] C. Guillaud, J. Phys. Radium **12**, 223 (1951)

[13] Heraeus QuarzGlas, Base Materials, Texas: Heraeus-QuarzGlas, March 01, 2014, Heraeus-QuarzGlas, Heraeus, Online, May 5, 2014.

[14] F. Heusler, Z. angew. Chem. **1**, 260 (1904)

[15] S. Hilpert and T. Dieckmann, Ber. Deut. Chem. Ges. **44**, 2831, (1911).

[16] M. G.Kanatzidis, R. Pottgen, W. Jeitschko, Angew. Chem. Int. Ed., 6996-7023 (2005)

[17] A. Kwiatkowski, D. Wasik, P. Dluzewski, J. Borysiuk, M. Kaminska, A. Twardowski and J. Sadowski, J. Magn. Magn. Mater. **321**, 2788-2791 (2009)

[18] J. Mira and J. Rivas, Modern Physics Letters B, **18**, No. 15, 725-747 (2004)

[19] F. C. Nascimiento, A. O. dos Santos, A. de Campos, S. Gama and L. P. Cardoso, Materials Research **9**, No. 1, 111-114 (2006)

[20] J. Nickels, Hewitt-Packard Manuscript (1995)

[21] J. Paitz, Krist. Tech. **7**, 999-1005 (1972)

[22] C. Petrovic, P. G. Pagliuso, M. F. Hundley, R. Movshovich, J. L. Sarrao, J. D. Thompson, Z. Fisk, and P. Monthoux, J. Phys. Condensed Matter **13**, L337-L342 (2001)

[23] L. Pytlik and A. Zieba, J. Magn. Magn. Mater. **51**, 199-210 (1985)

[24] A. Smits, H. Gerding, and F. VerMasst, Z. Physik. Chem. **357** (1931)

[25] B. T. Willis and H. P. Rooksby, Proc. Phys. Soc. B **67**, 290 (1954)

[26] R. H. Wilson and J. S. Kasper, Acta. Cryst. **17**, 95 (1964)

[27] B. D. White, K. Huang, I. K. Lum, J. J. Hamlin, S. Jang, G. J. Smith, J. W. Simonson, C. S. Nelson, M. C. Aronson, and M. B. Maple, (submitted May 2014)

[28] A. Zieba, Y. Shapira and S. Foner, Physics Letters **91A**, No. 5, 243-245 (1982)

[29] A. Zieba, R. Zach, H. Fjellvag and A. Kjekshus, J. Phys. Chem. Solids **48**, No.1, 79-89 (1987)

IV

Introduction to $\mathrm{CeCoIn_5}$

Many f - electron materials exhibit an array of strongly correlated electron behavior. These materials often display phenomena such as heavy fermion behavior, Kondo coherence, unconventional superconductivity, deviations from the Landau fermi liquid model, and quantum criticality. For example, in the CeMIn$_5$ (M = Co, Ir, Rh) family, several of these phenomena are believed to be present. To further probe the underlying mechanisms of these complex interactions several different experimental methods such as chemical substitution, applied pressure, and magnetic fields have been used. The results displayed complex experimental observations. In particular, the study of CeCoIn$_5$ has been important in understanding the role of quantum criticality in unconventional superconductivity and deviations from the fermi liquid picture. This study probes the interactions of the magnetic Ce ion by attempting to chemically substitute ytterbium, the hole-doped analogue to cerium, into the parent compound CeCoIn$_5$.

Since its discovery in 2000, CeCoIn$_5$ remains a heavily studied system. This system has provided an excellent platform to study the relationship between superconductivity and quantum criticality [16], and serves as a possible heavy fermion analogue to the high T_c cuprates [12, 18] due to its d-wave symmetry [1, 6]. CeCoIn$_5$ exhibits a plethora of exotic behavior including unconventional superconductivity, Kondo behavior, non-fermi liquid behavior and quantum criti-

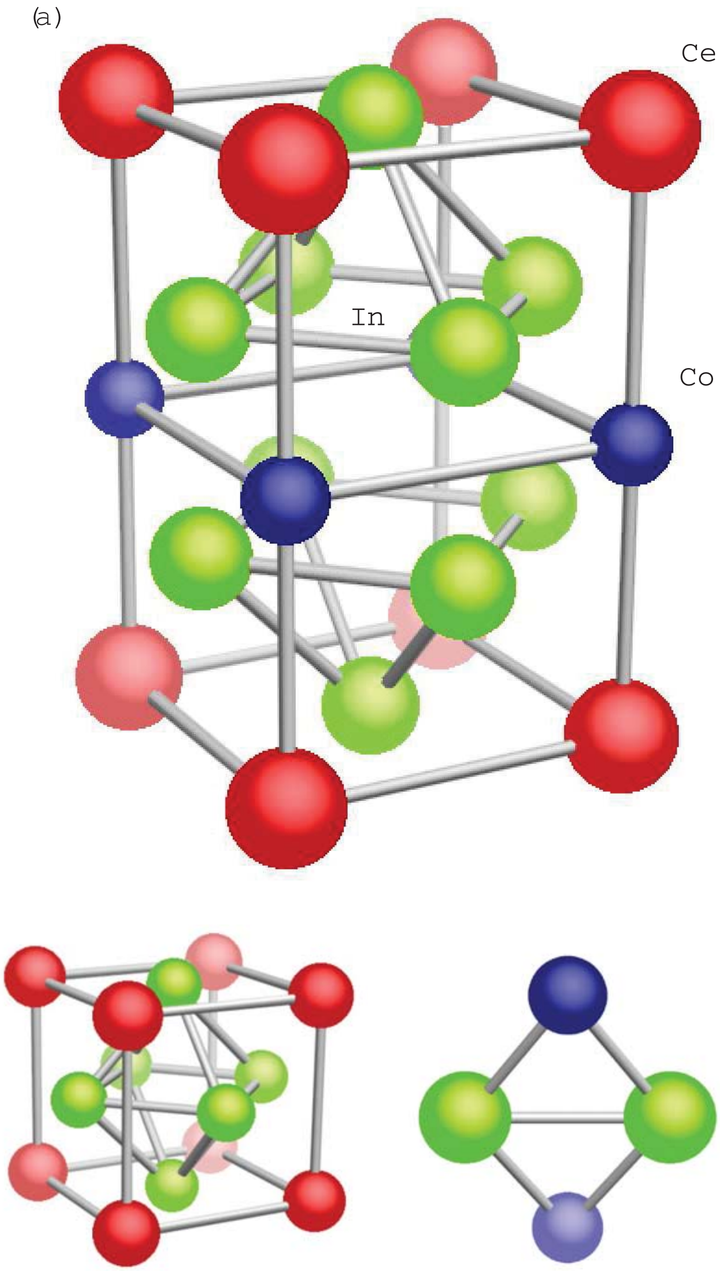

Figure IV.1: (a)Crystal structure of $CeCoIn_5$ (b) $CeIn_3$ structure and (c) $CoIn_2$. For all the crystal structures the red atoms represent Cerium, the green atoms represent Indium and the blue atoms represent Cobalt.

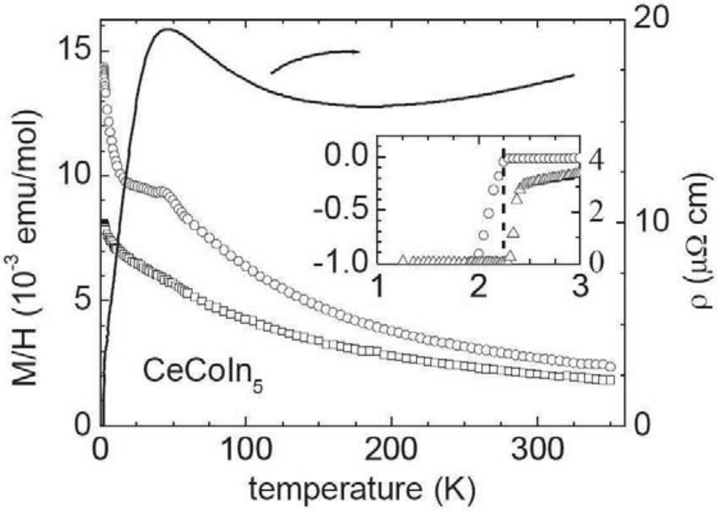

Figure IV.2: Magnetic susceptibility and resistivity measurements of CeCoIn$_5$ taken from [12].

cality. It is our goal here to further probe this system by the chemical substitution of nonmagnetic impurities at low concentrations and institute a more complete investigation of the effects of ytterbium on CeCoIn$_5$.

Within the CeMIn$_5$ (M = Ir, Rh Co) family and Ce-based HFSC, CeCoIn$_5$ has the highest transition temperature (T_c = 2.3K) to a superconducting state at ambient pressure. The CeMIn$_5$ family consists of layered crystal structure and crystallizes in the tetragonal space group $P4/mmm$. CeCoIn$_5$ forms in a quasi-2D HoCoGa$_5$ crystal structure with alternating layers of CeIn$_3$ and CoIn$_2$ as seen in Fig. IV.1 (Lattice constants a = 4.62 Åand c = 7.56 Å[7]).

The magnetic susceptibility is anisotropic with fields applied ∥ and ⊥ to the ab plane. Here χ is larger when the field is ⊥ to the ab plane. It is demonstrated in Fig. IV.2 that $\chi \perp ab$ saturates at approximately T ∼ 50 K, which is analogous to the Kondo temperature seen in resistivity. Below the saturation, the magnetic susceptibility shows a sharp upturn. However, there is no magnetic ordering is seen in the temperature range 1.8 K < T < 300 K. The effective magnetic moment for the material is $\mu_{eff} = 2.9\mu_B$ and the Curie Weiss temperatures are θ_{CW} = -87 K and θ_{CW} = -54 K for fields applied ∥ and ⊥ to the ab plane, respectively [12].

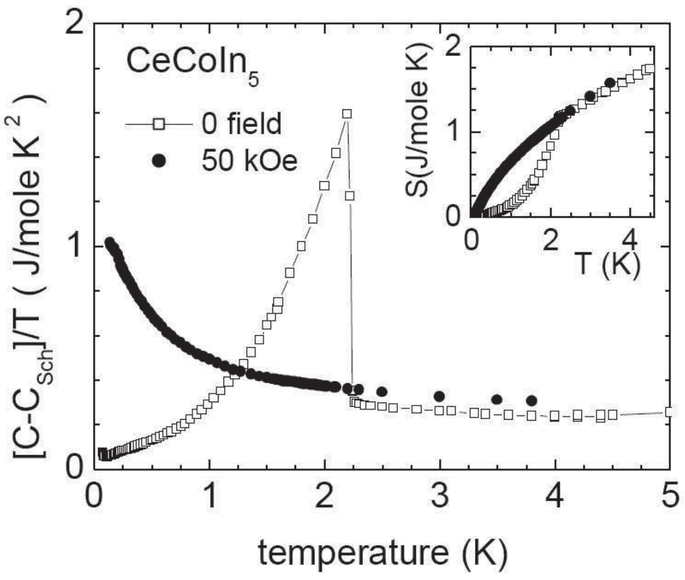

Figure IV.3: Specific heat measurements with the contributions due to Schottky anomaly already subtracted under zero field and 50 kOe; the inset shows the calculated entropy of $CeCoIn_5$ [12].

The resistivity ρ is weakly temperature dependent until a characteristic coherence temperature T_{coh} after which the a rapid decrease occurs. The resistivity ρ deviates from the the Fermi liquid model, such that it is linear in temperature ($\rho \sim$ T) below 20 K. Typical values for ρ_0 range from 2 - 6 $\mu\Omega$cm. The specific heat is shown in fig. IV.3 and shows $C/T = 290$ mJ mol^{-1}K^{-1}, indicating it is a HF system and mass renormalization occurs. According to Tinkham strong coupling occurs in systems where $\Delta C/\gamma T_c = 1.43$ [19], for $CeCoIn_5$ we see $\Delta C/\gamma T_c = 4.5$ [12]. This indicates extremely strong coupling. Kim et al. made specific heat and susceptibility measurements and found that both quantities deviate from the fermi liquid model [9], such that $C/T \propto$ -ln$T$ and $\chi \propto T^{-0.4}$. Although long range antiferromagnetic order is not observed in $CeCoIn_5$, these results indicate that the system is close to an antiferromagnetic quantum critical point at $P = 0$.

The possibility of superconductivity developing near a quantum critical point lead to pressure and magnetic field studies of the system to confirm this belief.

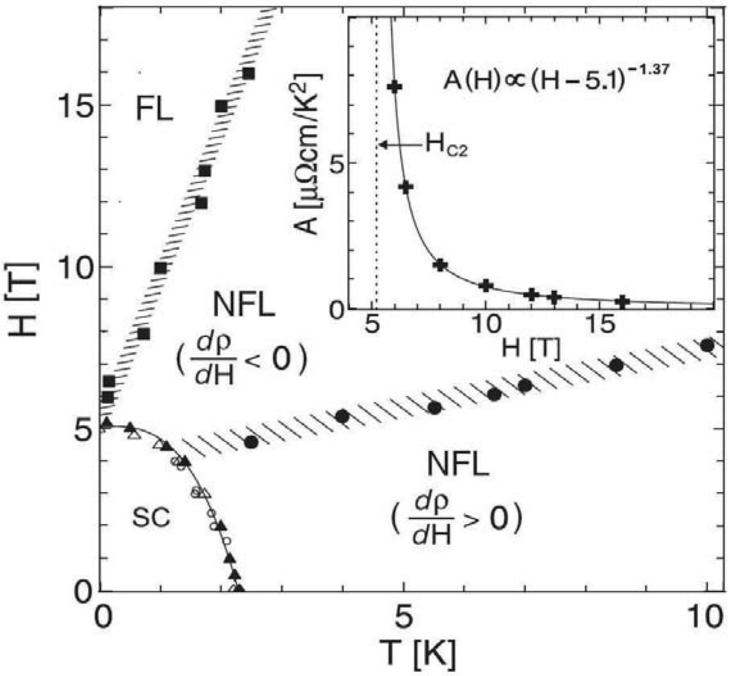

Figure IV.4: Field - temperature phase diagram of $CeCoIn_5$, where NFL is non fermi liquid with positive and negative regimes for magnetoresistance, FL is fermi liquid. The inset shows the field dependence of the coefficient A from the power law fit $\rho(T) = \rho_0 + A\mathrm{T}^n$ [11].

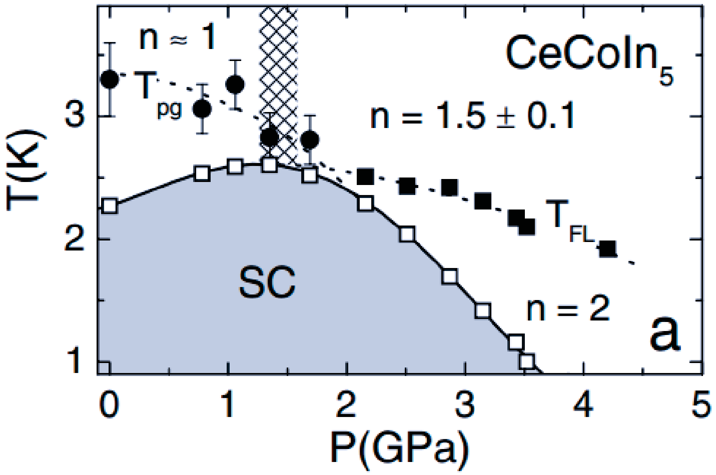

Figure IV.5: (a) Pressure - temperature phase diagram of $\mathrm{CeCoIn_5}$, where NFL is non fermi liquid regime with power law dependence, 1≤n≤ 1.5, FL is fermi liquid, SC is superconductivity and PG is pseudogap. [11]

Sidorov et al. [16] studied the effects of pressure on resistivity and found that the transport and thermodynamic properties are controlled by an antiferromagnetic critical point, such that P_c is an inaccessible negative pressure, as indicated by the phase diagram in Fig.IV.5. Another interesting point is that the non-fermi liquid behavior is exhibited in the normal state, persisting to high pressures of approximately $P \sim 1$ GPa and is not driven to a fermi liquid state until $P > 2$ GPa. Paglione et al. [11] also observed the suppression of non-fermi liquid behavior, but with the application of a magnetic field. Providing evidence for a field induced quantum critical point in $\mathrm{CeCoIn_5}$. Resistivity measurements were made down to 20 mK and magnetic field up to 16 T and the results were intriguing. Complex field dependence of of the normal state properties were observed, persisting to high fields and fermi liquid behavior was only observed in small region of extremely high fields and low temperatures.

V

$Ce_{1-x}Yb_xCoIn_5$ Experimental Details

V.A Elemental Preparation

The compounds in this thesis were synthesized via flux growth to produce high quality single crystals. The melting temperatures, suppliers and purities are listed in table V.A. Preliminary cleaning and cutting were necessary for the rare earths prior to synthesis and are described in this section. Single crystals of $Ce_{1-x}Yb_xCoIn_5$ were formed in molten indium, using the molten metal flux technique [8, 12, 20].

The Cerium, a 0.5 in diameter cylindrical ingot stored in a pyrex ampoule under half an atmosphere of argon, was cut with a handsaw into slices approximately 0.12 in thick (1.5 mm). When the slice was obtained the cerium ingot was then sealed again in a pyrex ampoule under argon. This practice ensured the cerium did not oxidize any more than necessary, but also that the same cerium was used throughout the substitution study. Once slices of Cerium have been isolated a two-part chemical etching process was quickly employed, again to minimize the amounts of oxide introduced to the system. First, the cerium slice was dipped into a solution of 1:3 hydrochloric acid to deionized water for approximately 5 seconds and thoroughly rinsed in deionized water afterwards. This removes a green layer of oxide and creates a black shell layer which is easily removed during the second stage, but is difficult to remove via mechanical brushing. The second solution contains mostly deionized water and just enough nitric acid to have a slow and controlled etch. Typically, this ratio is about 1:15 by volume but depends on the amount of exposed surface area of the cerium. During the chemical treatment one can observe the black cerium shell dissolving leaving the cerium. This process alone can take up to two minutes. Once thoroughly rinsed with water this leaves the cerium without any traces of oxidation and can be safely stored in an alcoholic solvent for half an hour before acidic treatment again becomes necessary. Any remaining residue can be easily and quickly removed manually with a wire brush. The etch takes less than ten percent of the initial mass, but can dissolve the cerium entirely if abandoned.

The Ytterbium pieces were stored in mineral oil within an evacuated desiccator such that the mineral oil can be removed with cycles of sonicating for five minutes in an alcoholic solvent such as ethanol. Although clean from mineral oil particular Lanthanides react strongly with oxygen and form thick, green layers of oxidation when exposed to atmosphere for extended periods of time so care was taken throughout to minimize exposure. The ytterbium pieces were cut down to a rectangular shape approximately 0.08 in x 0.08 in. Cobalt and Indium are fairly resistant to oxidation so no special precautions are required as in the cases for the rare earths. The cobalt pieces were cut with bolt cutters to no larger than 0.08 in and the indium tear drops were cut into four pieces.

Ce pieces, Yb pieces, Co pieces and Indium shot were stoichiometrically weighed out according to the desired concentrations of Yb substitution. The ratio of flux, based on the parent compound, is 1:15. This ratio was determined in order to prevent the formation of $CeIn_3$ as seen in the phase diagrams depicted in fig. V.1. Since the cerium reacts quickly in atmosphere, it is treated as a limiting factor and weighed first. The weights of the other constituents were recalculated

Table V.1: Melting temperatures, supplier, and purities of elements used in this thesis

Element	Melting Temp. (°C)	Supplier	Purities
Ce	800	Alfa Aesar	4N
Yb	819	Alfa Aesar	4N
Co	1495	Alfa Aesar	4N
In	156	Alfa Aesar	4N

based off the cerium mass and weighed to within 0.05 mg of the desired mass. The indium, due to its function as a flux metal, was only weighed out to within 0.5 g of the target mass. After obtaining the mass the cerium slice was cut into sixteen volume-equivalent pieces, each piece about 0.1 in x 0.1 in. All the pieces were reweighed to ensure consistency then rinsed and stored in acetone. In order to assist in homogeneous melting and reaction whilst annealing all the constituents were cut to be approximately the same size, 0.08 in (2 mm). The diameter of the smaller alumina crucible is roughly 0.55 in so all metals were cut to less than half this size. This size was empirically determined to optimize the crucible assembly, the quantity and quality of desired crystals. Larger alumina crucibles reproducibly yield. However, if the crystals grow too large excess indium becomes trapped within the layers of the crystal. The excess of indium is one of the major obstacles to producing reliable and clean data for any of the measurements.

V.B Flux-Growth of Single Crystals $Ce_{(1-x)}Yb_xCoIn_5$

Though I have synthesized this compound across the entire regime for x (x= 0.0, 0.01, 0.02, 0.03, 0.05, 0.10, 0.125, 0.15, 0.20, 0.225, 0.25, 0.3, 0.4, 0.5, 0.6, 0.65, 0.7, 0.75, 0.75, 0.8, 0.9, 0.97, 0.98, 0.99, 1.0), the measurements performed and described here account for only a fraction of the ongoing work.

Once the constituents were prepared and weighed out they were placed in layers within an alumina crucible (99.7% Al_2O_3, 3 in long, closed one end, (3/8" ID, 1/2"OD),which can hold approximately 15g of indium. When larger alumina

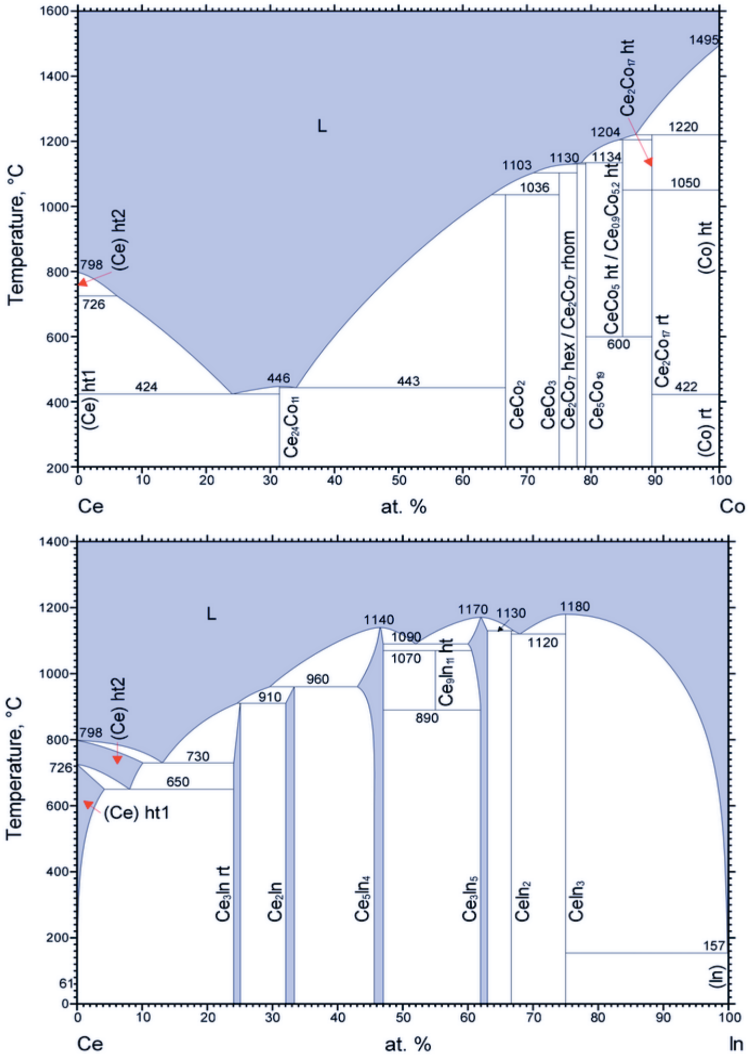

Figure V.1: Phase diagram of (a) Ce - In [10]and (b) Ce - Co[17].

crucibles were used, (5/8" ID, 1" OD), the crucibles held approximately 45 g of indium. Approximately half of the indium was packed with a metal rod into the bottom of the crucible. The rare earth's and transition metal Co were added and the remaining indium was pact on top to ensure the elements were secure. The remaining space (approximately 1/2") was filled with quartz wool, which would serve as a sieve to spin off the excess indium in the centrifuge. The packed crucible was then placed in quartz ampoule (14 mm x 16 mm or 27 mm x 30 mm) and a hydrogen/oxygen flame was used to shape the quartz into two chambers separated by a thin capillary approximately 1" above the crucible. The quartz ampoule was placed on a vacuum line and evacuated to 20 - 30 mtorr using mechanical vacuum pump and refilled with argon gas five times to remove oxidizing atmosphere. An oxygen/hydrgen flame was used to seal off the crucible in a partial pressure of 150 torr of argon to avoid over pressurization at higher temperatures and the ampoules were placed, in groups of four, into a 1200○ C Lindberg resistive heating box furnace at a 60° angle. Many of the crystal nucleate at the crucible wall so a perfect vertical or horizontal placement will minimize the potential size of the crystals. Orientations close to 60° balance well the nucleation sites with the vertical space in which the crystals can expand. Also, slight temperature gradients within the furnace which were recorded and taken into account during placement of the samples.

Although this particular heating curve deviates from previously published results [12], it was the most effective in producing large single crystals throughout the doping series. Initial heating rate of 50 ° C/hr was chosen to allow homogenous heating within the furnace. Once the furnace reached 1050° C the samples dwelt there for 72 hours, allowing the starting constituents sufficient time to dissolve in the molten metal. A two stage cooling process was chosen to prevent the formation of thermodynamically meta-stable binary compounds, due to the eutectic formed by Cerium and Cobalt as seen in fig. IV.2. First, the furnace cooled at a rate of 20° C/hr until 800° C when the ramp rate changed to a slow cool at 2° C/hr until 450°

C. If one assumes nucleation occurs during the high temperature dwell at 1050° C then this two step cooling trend is when the samples crystallize out of the indium solvent. The furnace was allowed to dwell for one more day at 450° C ensuring all systems inside were at thermal equilibrium. Once the furnace reached 450° C, the quartz ampoules were removed one at a time from the furnace and carefully placed upside down in a centrifuge. The quartz wool served as a sieve and separated the single crystals from the excess flux as it was spun off in the centrifuge. The quartz was allowed to cool then broken with a hammer. The alumina crucible was removed from the quartz and the crystals were mechanically removed by scraping and etching with a dilute solution of HCl. To ensure the crystals were free from excess Indium small batches of crystals were etched in a 1:20 HCl:H_2O for several hours then rinsed. The clean samples were separated and the process repeated as necessary. The dilute solution was useful because the HCl etched the Indium without etching the desired single crystals themselves. The $CeIn_3$ binary has the same basic structure and tends to form in copious quantities. This complicates the isolation process, but fortunately the $CeIn_3$ binaries are not as resistant to the chemical process. One can observe square pits and surface deformations in the pure binary as opposed to the fully developed 115 structure which does not show any evidence of degradation. Prior to measurement the individual crystals are etched in pure HCl for no more than 30 seconds at a time. The crystals are fairly resistant to hydrochloric acid but any longer and preferential etching in the form of small cube-like pits can be observed. An example of an etched single crystals is seen Fig. V.2.

V.C Basic Characterization

V.C.1 X-ray Diffraction

Thin tetragonal shaped crystals, representative of the samples within the batch, were collected and etched in acid to remove excess Indium flux from the

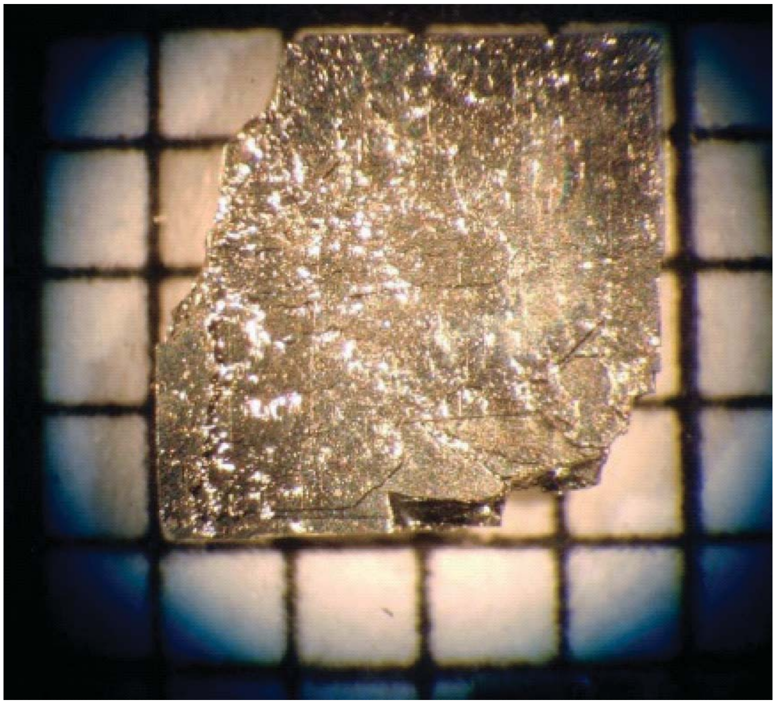

Figure V.2: Example of a single crystal and its dimensions

surface. To verify the structural character and composition of each growth powdered diffraction technique for measurement preparation were employed. Several single crystals were collected and ground using an agate mortar and pestle. A clean glass slide with three layers of tape positioned around the center of the slide served as the vehicle for measurement. The powder was mixed with petrolatum jelly to form an opaque paste and placed on the prepared glass slide. Another clean glass slide was used to smooth the surface of the paste and the tape was removed before any measurements were taken. X-ray powder diffraction measurements were completed on a commercial Bruker AXS Discover D8 x-ray diffractometer at room temperature. The intensity was measured as a function of 2θ from 19° - 93° using Cu Kα_1 radiation.

One of the ongoing investigations into the nature of $\mathrm{CeCoIn_5}$ is the dilemma of valence fluctuations upon rare earth substitution. Energy-dispersive X-ray spectroscopy(EDS, EDX, or XEDS), sometimes calledenergy dispersive X-ray analysis (EDXA) or energy dispersive X-ray microanalysis (EDXMA), is an analytical technique used for the elemental analysis or chemical characterization of a sample. It relies on the interaction of some source of X-ray excitation and a sample. Its characterization capabilities are due in large part to the fundamental principle that each element has a unique atomic structureallowing unique set of peaks on its X-ray spectrum. To stimulate the emission of characteristic X-rays from a specimen, a high-energy beam of charged particles such as electrons or protons, or a beam of X-rays, is focused into the sample being studied, represented by the square in the top picture of figure V.3. At rest, an atom within the sample containsground state(or unexcited) electrons in discrete energy levels orelectron shellsbound to the nucleus. The incident beam may excite an electron in an inner shell, ejecting it from the shell while creating anelectron holewhere the electron was. An electron from an outer, higher-energy shell then fills the hole, and the difference in energy between the higher-energy shell and the lower energy shell may be released in the form of an X-ray. The number and energy of the X-rays emitted from a specimen can be measured by an energy-dispersive spectrometer. As the energy of the X-rays are characteristic of the difference in energy between the two shells, and of the atomic structure of the element from which they were emitted, this allows the elemental composition of the specimen to be measured. However, due to the reliant nature of the analysis on both the energy of the excitation plus the number of excitations detected, inconsistencies can introduce large error bars into data that can be maximized if the user is inattentive to the measurement and results. The results are charted in spectrographs plotting intensity in arbitrary units and the energy of the excitations up to 7.5 keV. The graphs shown in the middle and the bottom of figure V.3 are for $\mathrm{Ce_{0.9}Yb_{0.1}CoIn_5}$ and $\mathrm{Ce_{0.9}Yb_{0.1}CoIn_5}$. In the case of Yb, the spectral lines defining the rare earth are very similar to other elements, like potassium. It is left to the user to identify which elements are to be included in the chemical analysis and which are to be ignored. These inconsistencies can further be exacerbated by differences in the synthesis techniques employed. In an effort to determine the extent to which the ytterbium was actually

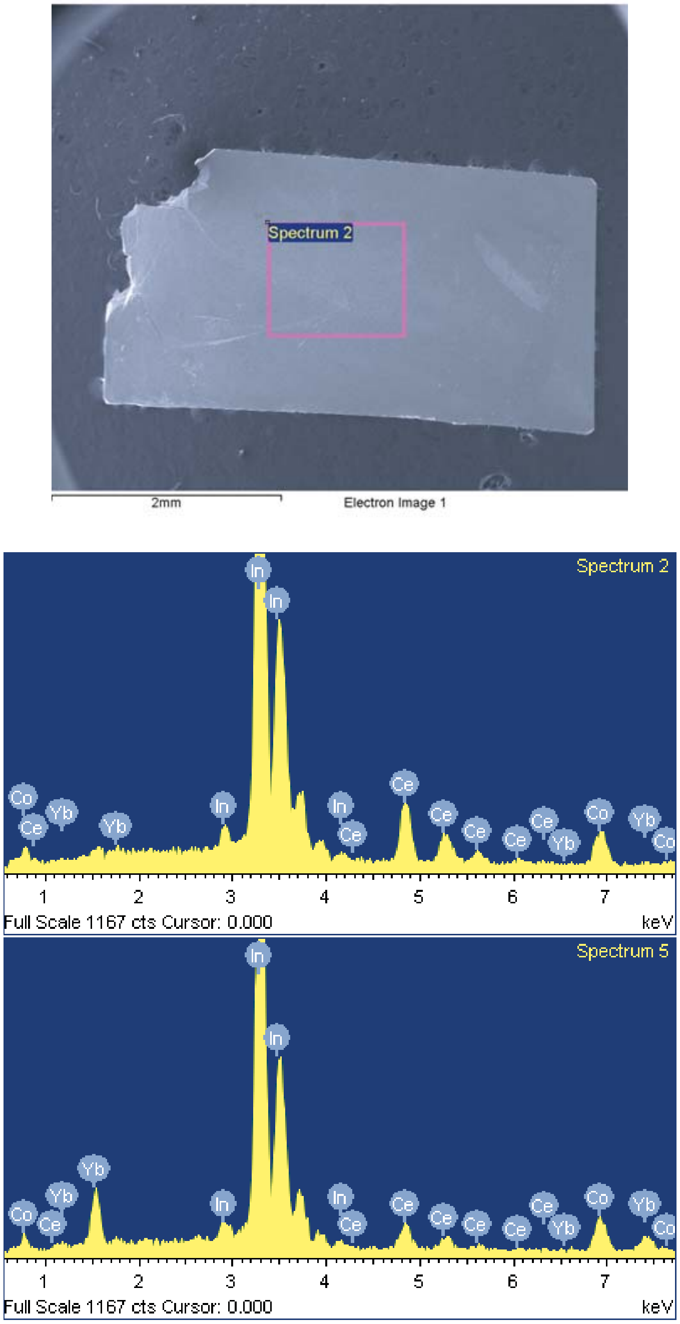

Figure V.3: (top) XEDS picture of representative target location for $Ce_{0.9}Yb_{0.1}CoIn_5$; (middle) Representative graph of the measured excitations for $Ce_{0.9}Yb_{0.1}CoIn_5$; (bottom) Representative graph of the measured excitations for $Ce_{0.5}Yb_{0.5}CoIn_5$

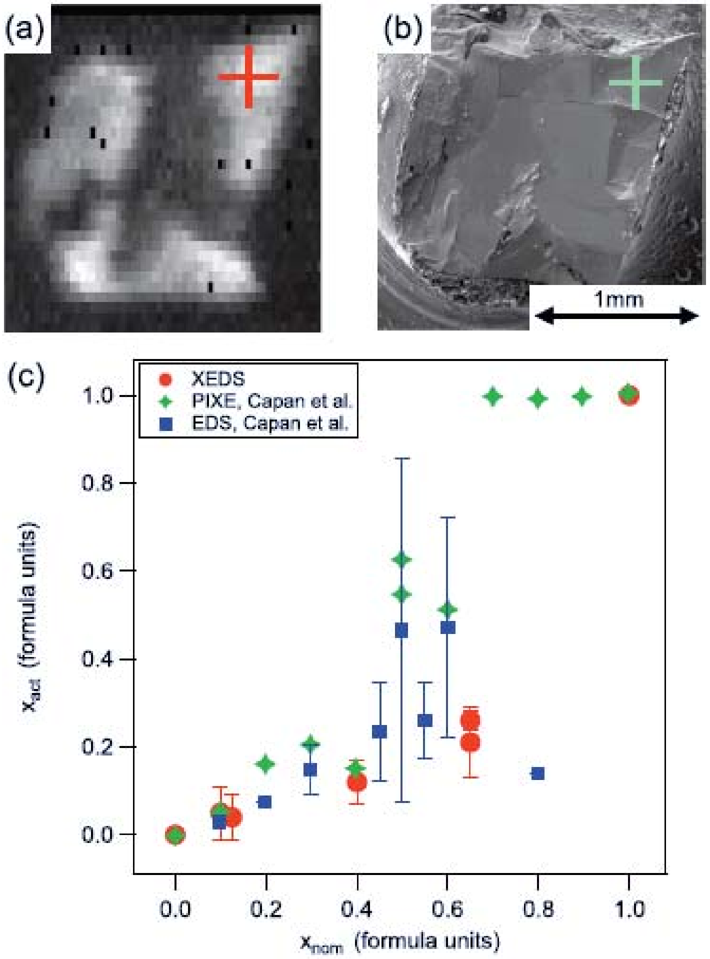

Figure V.4: (a) XEDS pictures taken under an optical microscope of representative target location marked with an “X”. The brighter spots indicate higher intensity of photoelectrons; (b) electron microscope picture of the same crystal, also marked at the scanned location; (c) Measured results of actual vs. nominal concentration also compared with data from Capan [3].

replacing the cerium at the rare earth sites several crystals from several batches covering the entire concentration range were measured. The results of these scans were then compared with the photoemission and x-ray absorption measurements described in the next section.

V.C.2 Photoemission and x-ray absorption

The electronic structure of $\mathrm{Ce}_{(1-x)}\mathrm{Yb}_x\mathrm{CoIn}_5$ ($x = 0.0$, 0.1, 0.2, 0.4, 1.0) has been studied by a combination of photoemission, x-ray absorption, and bulk property measurements. The spectroscopic measurements XAS, XPS, and ARPES were performed at undulator beamline 7.0.1 of the Advanced Light Source (ALS) synchrotron. XAS, x-ray absorbtion spectroscopy, was measured using total electron yield (TEY), by simultaneously measuring the sample current and the reference of a Ni mesh located before the sample in the monochromator. A Scienta R4000 electron spectrometer with 2D parallel detection of electron kinetic energy and angle in combination with a highly automated six-axes helium cryostat goniometer was used to acquire Fermi surface (FS) and electronic structure maps with a wide 30° angular window covering multiple Brillouin zones. The measurements were performed with pressure between 8 x 10^{-11} and 1 x 10^{-10} mbar. The samples were cleaved in situ by pushing against a post which was glued on the sample surface by epoxy adhesive. The cleavage temperature was between 20 and 25 K, essentially equal to the measurement temperature, which was 25 K for CeCoIn_5 and 20 K for YbCoIn_5. The position of the Fermi energy and the energy resolution were determined by measuring a gold foil adjacent to and in good thermoelectrical contact with the sample. Before measuring, the gold foil was scraped in situ to obtain a clean surface. Within about 100 μm, all spectroscopic data were collected on the same spot of the cleavage plane, which showed no visible inhomogeneities either in situ or afterwards in images under both an optical microscope and an electron microscope, top left and right of figure V.4, respectively.

XAS measurements had a resolution of 250 meV. For XPS, x-ray photo-

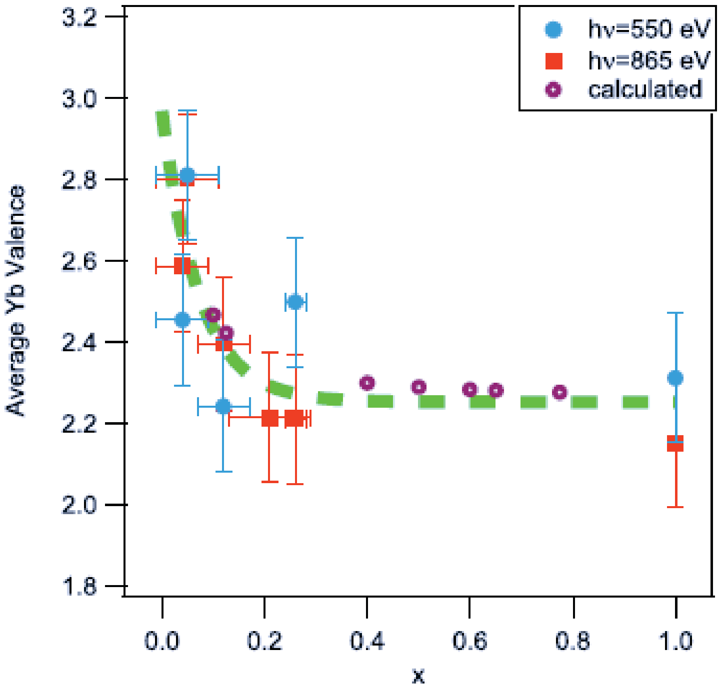

Figure V.5: Example of a single crystal's energetic spectrum as measured and analyzed by x-ray photospectroscopy. These results can be compared to the results of the XEDS measurements as seen in table V.C.2.

electron spectroscopy, the overall energy resolution was set to 140 meV FWHM for photon energies of hν = 550 eV and 250 meV for photon energies of hν = 865 eV. For ARPES, angle resolved photoemission spectroscopy, the total energy resolution of the analyzer and exciting photons varied from 30 meV at hν = 80 eV to 45 meV at hν = 200 eV, and the angular resolution of 0.3° corresponds to a parallel angular momentum resolution range of 0.024 to 0.037 Å^1. Detector angular distortions are corrected using calibration data acquired with a slit array placed between the sample and analyzer lens. Angular and photon-dependent Fermi-energy maps were extracted with an energy width of 50 meV. The value of k perpendicular to the sample surface (k_z) could be selected by varying the photon energy, as verified and calibrated from repeating features in k_z-k_x maps using a standard method that approximates the photoelectron dispersion by a free

Table V.2: Results of the XEDS analysis for $Ce_{(1-x)}Yb_xCoIn_5$; nominal concentrations shown on top with measured values displayed in table.

	Nominal concentration x_{nom}						
Element	0	0.1	0.125	0.4	0.65	0.65	1
Ce content	1.00	1.01	1.01	0.93	0.77	0.87	0.00
Yb content	0.00	0.04	0.04	0.11	0.24	0.19	0.92
x_{act}	0.00	0.04	0.04	0.12	0.26	0.21	1.00
Δx_{act}	0.00	0.05	0.05	0.05	0.03	0.08	0.00

electron parabola and an“inner potential V_0 to characterize the surface potential discontinuity [5]. A V_0 value of 11.9 ± 0.6 eV best describes the repeating features in the data.

Previous findings of a Ce valence near 3+ for all concentrations and of a Yb valence near 2.3+ for $x \geq 0.3$ to 1.0 were confirmed. One new result of this study is that the Yb valence for $x \leq 0.2$ increases rapidly toward 3+ with decreasing concentrations of x, which correlates well with de Haas van Alphen results showing a change of Fermi surface around $x = 0.2$ [13]. Another new result is the direct observation by angle resolved photoemission Fermi surface maps of $\approx$ 50% cross-sectional area reductions of the α and β sheets for $x = 1$ compared to $x = 0$, and a smaller, essentially proportionate, size change of the α sheet for $x = 0.2$. The significant finding for the ARPES data for $x = 0.2$ is that the -sheet areas are, even by eye, intermediate between those for $x = 0$ and 1. This can clearly be observed in the series of ARPES images in fig. V.6. Quantitatively, the change in area from $x = 0$ to 0.2 is 21% and 14% of the change from $x = 0$ to 1 for α_1 and α_2, respectively, i.e., roughly in the same proportion as the doping. Unfortunately, it is not possible to compare this result with the dHvA data for intermediate values of x. However, these changes are found to be in good general agreement with expectations from simple electron counting.

Since the synchrotron spectroscopy is performed with a small photon spot on a selected region of a cleaved surface, the XEDS analysis was performed after the synchrotron spectroscopy was done and great care was taken to obtain the

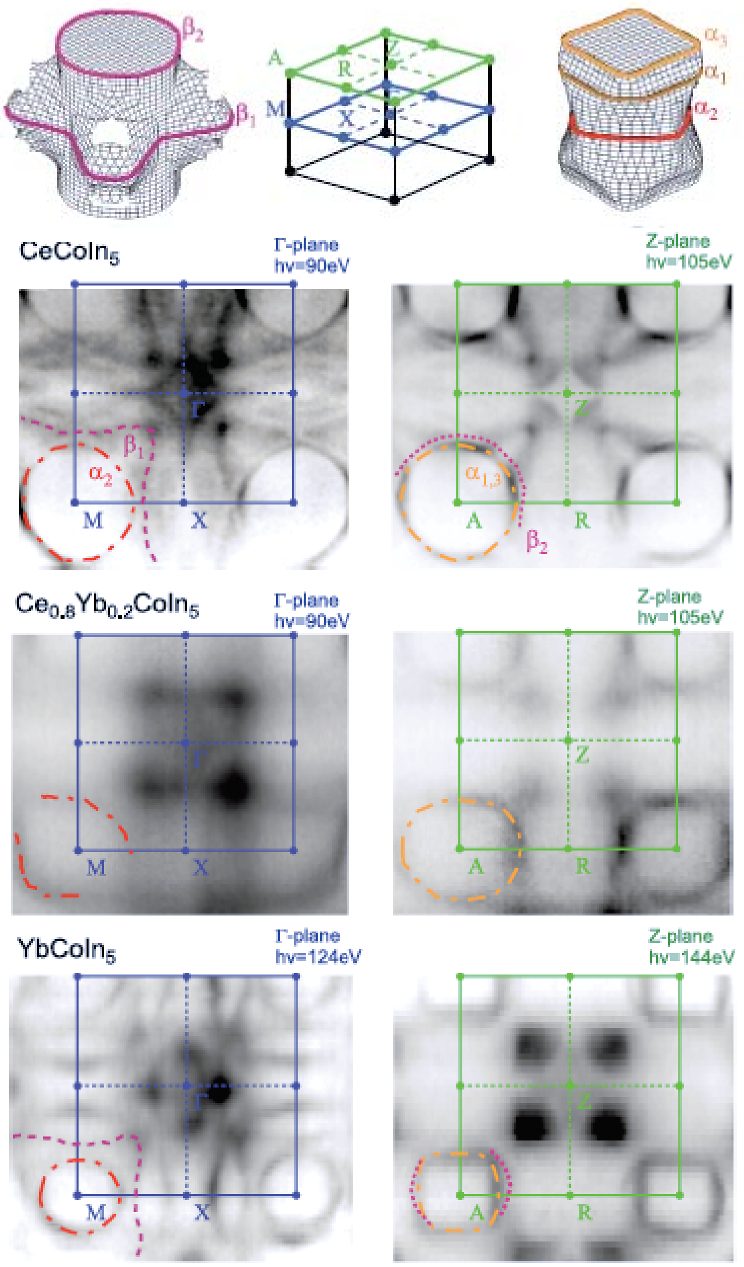

Figure V.6: Top image: Models of the Fermi surfaces investigated; Lower image: APRES images of parent compounds $\mathrm{CeCoIn_5}$ and $\mathrm{YbCoIn_5}$ and some representative mixed concentrations.

composition at the same location on the sample as that where the synchrotron spectroscopy was performed. Using the focused probe of the scanning electron microscope, it is possible to determine the composition of the sample with a resolution of a few micrometers. The actual value depends on the average atomic number of the sample and the accelerating voltage of the microscope, 30 kV in this case. Therefore by this method, we can detect inhomogeneities on the microscale but not the nanoscale range. As the photon beam-spot for the synchrotron spectroscopy was much larger, roughly 50 to 100 μm, we checked the microscale homogeneity by doing XEDS analysis around the measured position, at two or three points roughly within a circle of $100 - 200$ micrometers diameter. We detected no significant changes in the Yb compositions.

V.C.3 Magnetization

To confirm transition temperature and magnetic moment magnetization measurements $M(H, T)$ were performed in a Quantum Design (MPMS XL-7) SQUID magnetometer and verified in a Quantum Design MPMS3. To prepare for such measurements we used a standard clear straw and placed an etched single crystal face down on 3M 1/4 in Kapton tape. The mass of a single crystal used in these measurements ranged from m $\sim$ 1 - 10 mg. The tape was pulled through the length of the straw for H $\|$ ab plane and pulled through cross section of the straw for H $\|$ c. In both cases, we adjusted the tape so that the single crystal was at the approximate center of the straw. Basic M(T) measurements were measured from 1.9 K - 300 K under zero field cooled and field (500 Oe) cooled conditions. Fields were applied parallel and perpendicular to the c-axis. These measurements were primarily to check for consistency amongst batches.

The magnetic susceptibility of metals containing lanthanide ions that exhibit the Kondo effect or valence fluctuations can be described by a Curie-Weiss law in high-temperature limit. For the present situation, the effective magnetic moments of the Ce and Yb ions are expected to be close to their Hunds rules values

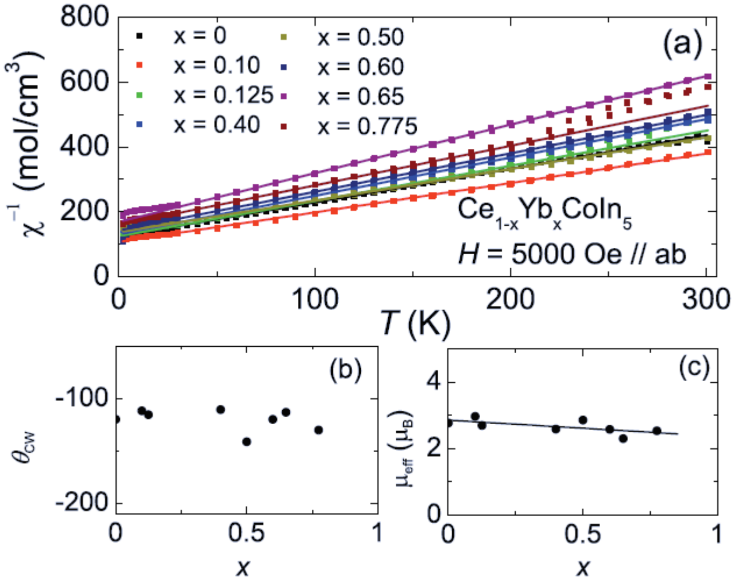

Figure V.7: Inverse magnetic susceptibility of $\mathrm{Ce}_{(1x)}\mathrm{Yb}_x\mathrm{CoIn}_5$ in the normal state as a function of Yb concentration, x [4].

corresponding to their f -electron configurations and the Curie-Weiss temperature represents a characteristic temperature associated with the Kondo effect for the trivalent Ce ions or valence fluctuations for the intermediate valent Yb ions. The Kondo and valence fluctuation temperatures are characteristic temperatures where the material gradually crosses over from a paramagnetic localized moment regime at high temperatures to a nonmagnetic Pauli-like regime at low temperatures. In the analysis, the magnetic susceptibility was taken to be a superposition of a Kondo contribution from the Ce ions and a valence fluctuation contribution from the Yb ions. The fact that Curie-Weiss temperature θ_{CW} is nearly independent of Yb concentration indicates that the energy scale associated with the combined Kondo and valence fluctuation contributions does not vary with Yb concentration. This is consistent with the stability of the correlated electron state in $\mathrm{Ce}_{(1-x)}\mathrm{Yb}_x\mathrm{CoIn}_5$ over a large Yb concentration range. Fig. V.7 (a) shows the inverse magnetic susceptibility $\chi_{ab}^{-1}\ (T) = H/M_{ab}(T)$ of $\mathrm{Ce}_{(1-x)}\mathrm{Yb}_x\mathrm{CoIn}_5$ in the normal state versus Yb concentration, x. The data were collected by warming the sample gradually

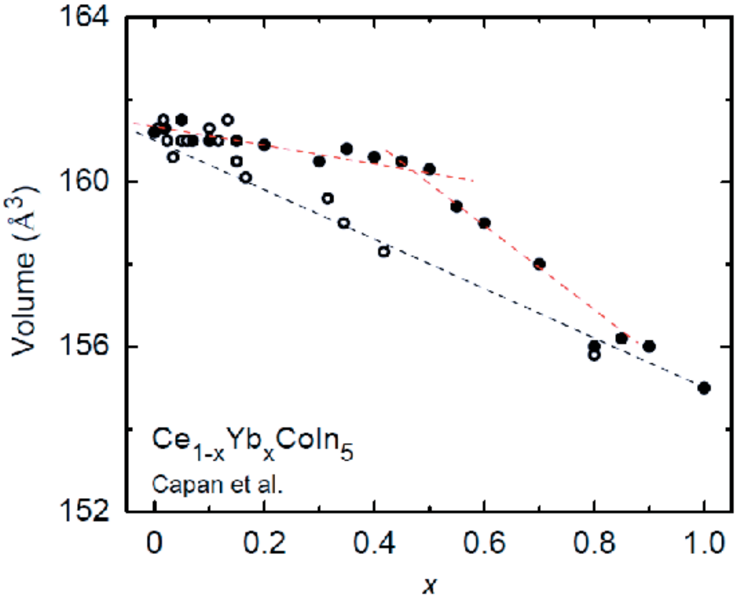

Figure V.8: EDS results from previous studies (filled circles) have been reinterpreted assuming Vegard's Law consistancy (black dashed line) and concentrations have been adjusted to reflect (unfilled circles)[3].

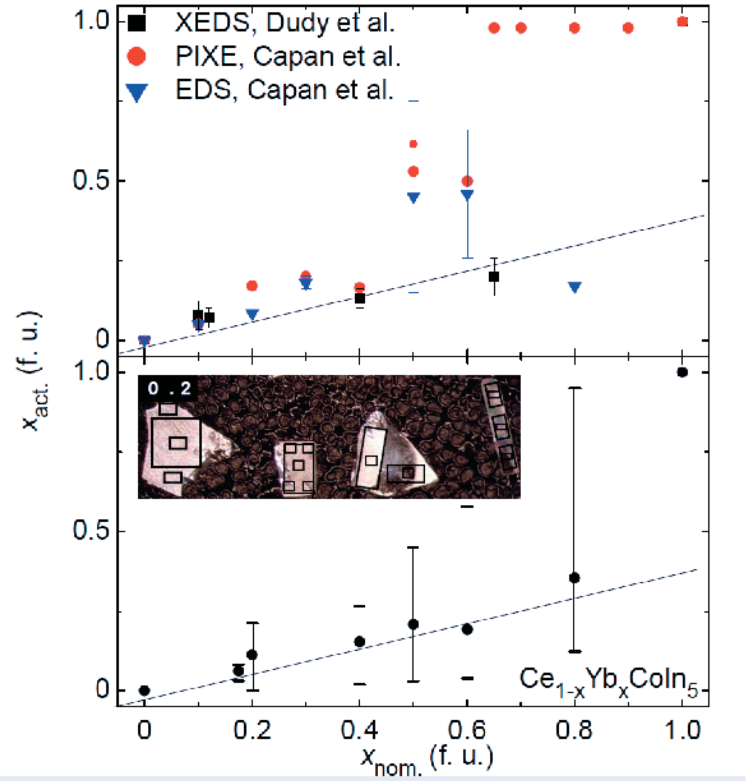

Figure V.9: EDS results as compared with Capan et al. [3]

after zero-field cooling (ZFC) and subsequently field cooling (FC). The difference between the ZFC and FC data is negligible. Above T ≈ 30 K and for all x, the magnetic susceptibility χ_{ab} of $\mathrm{Ce}_{(1-x)}\mathrm{Yb}_x\mathrm{CoIn}_5$ can be described well by a Curie-Weiss law,

$$\chi_{ab} = \frac{N_A \mu_{eff}^2}{3k_B(T\theta_{CW})} \tag{V.1}$$

as described before. The effective magnetic moment μ_{eff} and the Curie-Weiss temperature θ_{CW}, as determined from fits of the data to the equations above, are shown in Figs. V.7(b) and V.7(c). The fits yield $\theta_{CW} \approx 120$ K, independent of Yb.

V.C.4 Discussion

The superconducting critical temperature T_C, determined from measurements of $\rho(T)$, vs x for $\mathrm{Ce}_{(1-x)}\mathrm{Yb}_x\mathrm{CoIn}_5$ from the data published by Shu et al.

(filled circles) and Capan et al. (filled triangles) are plotted vs. Yb concentration, x [3, 15]. The unfilled circles and triangles indicate those same T_C values plotted as a function of $x_a ct$. The solid line indicates the evolution of T_C with x for thin film samples published by Shimozawa et al. [14].

The unit cell volumes V of the system $\mathrm{Ce}_{(1-x)}\mathrm{Yb}_x\mathrm{CoIn}_5$ from Capan et al. are plotted as a function of nominal Yb concentrations, x, and are represented by filled circles [3]. Dashed red lines are guides to the eye that are rough linear fits to the $V(x)$ data in three distinct Yb concentration regions. The unfilled circles indicate the adjusted x values; these values were calculated by adjusting the observed $V(x)$ data so that they are constrained to follow Vegards law, emphasized in fig. V.8 by the dashed black line [4]. This is currently a multi-collaborative and ongoing process with publications in the works.

Bibliography

[1] H. Aoki, T. Sakakibara, H. Shishido, R. Settai, Y. Onuki, P. Miranovic and K. Machida, J Phys. Condens. Matter **16**, L13 (2004)

[2] P.C.Canfield, Z. Fisk, Phil. Mag. B **65**, 1117-1123 1992

[3] C. Capan, G. Seyfarth, D.Hurt, B. Prevost, S. Roorda, A.D.Bianchi, and Z. Fisk, Europhys. Lett. **92**, 47004 (2010).

[4] L. Dudy, J. D. Denlinger, L. Shu, M. Janoschek, J. W. Allen, and M. B. Maple, PRB **88**, 165118 (2013)

[5] F. J. Himpsel, Adv. Phys. **32**, 1 (1983).

[6] K. Izawa, H. Yamaguchi, Y. Matsuda, H. Shishido, R. Setta, and Y. Onuki, Phys. Rev. Lett. **87**, 5 (2001)

[7] Y. M. Kalychack, V. I. Zaremba, V. M. Baranyak, V. A. Bruskov and P. Y. Zavalij, Izy. Acad. Nauk. SSSR Met **1**, 209 (1989)

[8] M. G.Kanatzidis, R. Pottgen, W. Jeitschko, Angew. Chem. Int. Ed., 6996-7023 (2005)

[9] J. S. Kim, J. Alwood, G. R. Stewart, J. L. Sarro and J. D. Thomspon, Phys. Rev. B **64**, 134524 (2001)

[10] H. Okamoto, Binary Alloy Phase Diagrams **2**, 1071-1073 (1990)

[11] J. P. Paglione, M. A. Tanatar, D. G. Hawthorn, E. Boaknin, R. W. Hill, F. Ronning, M. Sutherland, L. Taillefer, C. Petrovic and P. C. Canfield, Phys. Rev. Lett**91**, 246405 (2003)

[12] C. Petrovic, P. G. Pagliuso, M. F. Hundley, R. Movshovich, J. L. Sarrao, J. D. Thompson, Z. Fisk, and P. Monthoux, J. Phys. Condensed Matter **13**, L337-L342 (2001)

[13] A. Polyakov, O. Ignatchik, B. Bergk, K. Gotze, A. D. Bianchi, S. Blackburn, B. Prevost, G. Seyfarth, M. Cote, D. Hurt, C. Capan, Z. Fisk, R. G. Goodrich, I. Sheikin, M. Richter, and J. Wosnitza, Phys. Rev. B **85**, 245119 (2012)

[14] M. Shimozwa, T. Watashige, S. Yasumoto, Y. Mizakami, M. Nakamura, H. Shishido, S. K. Gho, T. Terashima, T. Shibauchi, and Y. Matsuda, PRB **86**, 144526 (2012)

[15] L. Shu, R. E. Baumbach, M. Janoschek, E. Gonzales, K. Huang, T. A. Sayles, J. Paglione, J. OBrien, J. J. Hamlin, D. A. Zocco, P.-C. Ho, C. A. McElroy, and M. B. Maple, PRL **106**, 156403 (2011)

[16] V. A. Sidorov, M. Nicklas, P. G. Pagliuso, J. L. Sarrao, Y. Bang, A. V. Balatsky and J. D. Thompson, Phys. Rev. Lett **89**, 15 (2002)

[17] X. Su, W. Zhang and Z. Du, J. Alloys Compd.P **267**, 121-127 (1998)

[18] M. A. Tanatar , J. Paglione1 , S. Nakatsuji, D. G. Hawthorn1 , E. Boaknin, R. W. Hill1 , F. Ronning1 , M. Sutherland , Louis Taillefer, C. Petrovic P. C. Canfield, and Z. Fisk, Phys. Rev. Lett. **95**, 067002 (2005)

[19] M.Tinkham, Introductioon to Superconductivity, ch.1, (Dover, New York 1996)

[20] V. I. Zaremba, U. C. Rodewald, R. D. Hoffman, Y. M. Kalychak and R. Pottgen, Z. Anorg. Allg. Chem. **629**, 1157-1161 2003

VI

Measurements performed at Quantum Design

VI.A $\mathbf{La}_{(1-x)}M_x\mathbf{OBiS}_2$ (M = Hf, Th)

Though most of my graduate work was focused on single crystal synthesis and characterization I was afforded the opportunity to assist in other projects as well as a conduit for more precise measurements at Quantum Design. This chapter focuses solely on the joy of teamwork between Duygu Yazici, myself and Quantum Design and the resulting publication, "Superconductivity induced by electron doping in the system $La_{(1-x)}M_xOBiS_2$ (M = Ti, Zr, Hf, Th)" [12].

Within the past couple of years, superconductivity has been reported in the layered compound $Bi_4O_4S_3$ [7], prompting investigations into related family members, including LnO$_{(1-x)}$F$_x$BiS$_2$ (Ln = La, Ce, Pr, Nd, Yb)[1, 2, 3, 4, 6, 8, 10, 11]. This family is composed of superconducting BiS_2 layers and blocking LnO layers, with similar traits to the famous high T_c cuprates and pnictides, dubbed "1111" family of compounds [9]. In these cases, the nature of the authors' investigations was chemical manipulation of these layers in order to induce superconductivity by restructuring the electronic configuration. Chemical substitution of tetravalent elements (Th^{4+}, Hf^{4+}, Zr^{4+}, and Ti^{4+}) into the trivalent La^{3+} site

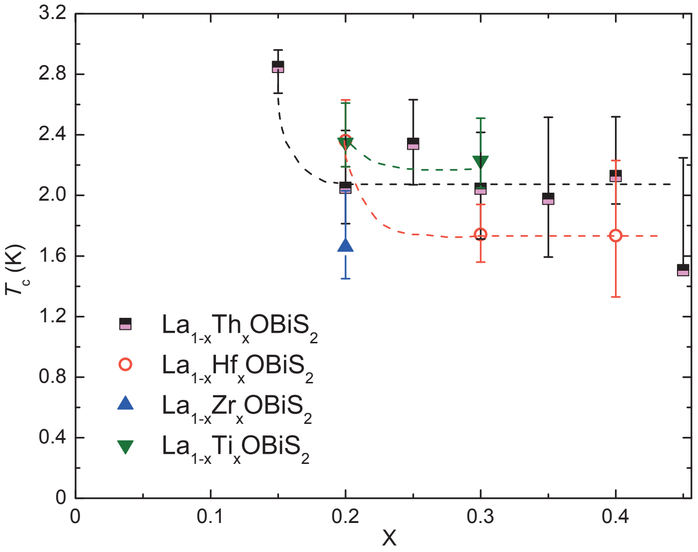

Figure VI.1: Resistive superconducting transition temperatures, T_c for $La_{(1-x)}M_xOBiS_2$ (M = Ti, Zr, Hf, Th) samples plotted against the nominal concentration, x. The value of T_c was defined where ρ drops to 50% of its normal state value. The vertical bars represent 90% and 10% of the normal state [12].

of $LaOBiS_2$ by means of solid state reaction was implemented in varying concentrations as a means of studying the effects of increasing the charge-carrier density, i.e. electron-doping, in the blocking layer. In order to understand the effects of the chemical substitutions, standard characterization was carried forth, including chemical analysis of composition and structure, electrical resistivity, magnetization and specific heat, from room temperature down to ∼ 1.8 K both with and without applied magnetic fields. Analysis revealed that while the parent compounds are bad metals superconductivity can be induced with transitions as high as 2.85 K for $La_{0.8}Th_{0.2}OBiS_2$ and 2.4 K for $La_{0.8}Hf_{0.2}OBiS_2$. As is the case with the "1111" family, superconductivity is only induced after a specific concentrations are doped into the material [9]. In the case of the Th-doped compound, superconductivity is seen in concentrations above $x = 0.15$. For the other substituted metals, superconductivity was seen after $x = 0.20$. From the phase diagram built, shown in figure VI.1, the superconducting transition temperatures, T_c, seem to suppress with increasing substitutions until $x = 0.45$ where the material starts to phase separate. However, the samples are suspected of having a poor homogeneity so if the error bars, which account for the 90% and 10% transitions, are taken into account one could easily argue that the transition temperatures are, in fact, concentration independent. Also, excepting the 15%-Th sample all of the transition temperatures are within 1.6 K - 2.4 K.

VI.B Low Temperature Measurements performed at Quantum Design

VI.B.1 Resistivity

In an attempt to understand the mechanism(s) behind superconductivity in these systems thermal sweeps of electrical resistance were performed under several applied fields ($H = 0$, 0.01, 0.05, 0.1, 0.2, 0.3, 0.4, 0.5, 1, and 9 T) down to 0.36 K. The resistivity curves have been normalized with the resistance at 5K and show a clear suppression of T_c with increasing applied fields. Both samples show a clear and sharp transition without an applied field while applied fields broaden the transition with increasing field. This is also analogous to the cuprates and the Fe-pnictide studies, though the mechanisms are still undergoing investigation[9]. In addition, as can be seen in Fig. VI.2 the upper critical fields have been calculated from the 90% and the 10% data, with the 50% transition shown as well.

VI.B.2 Heat Capacity

Heat Capacity measurements were also performed from 30 K to 0.36 K using the He-3 insert in a Quantum Design DynaCool for $La_{0.85}Th_{0.15}OBiS_2$ and $La_{0.8}Hf_{0.2}OBiS_2$. The main figures each plot the C/T vs. temperature T with insets showing C/T vs. T^2 in the upper left part of the figure and C_e vs. T in the inset in the lower right, where C_e/T is the electronic contribution to the specific heat in the vicinity of the superconducting transition. The red line in

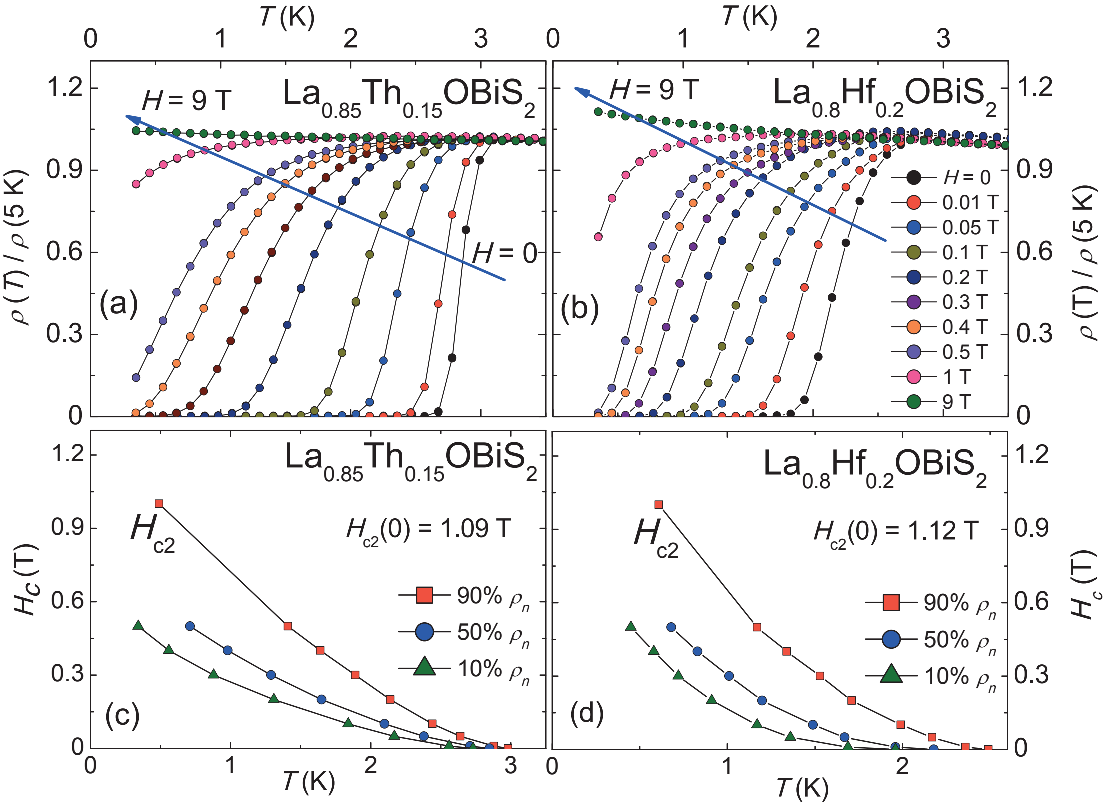

Figure VI.2: (a, b) Resistive superconducting transition curves for $La_{0.85}Th_{0.15}OBiS_2$ and $La_{0.8}Hf_{0.2}OBiS_2$ samples, respectively, measured under several different applied magnetic fields ($H = 0$, 0.01, 0.05, 0.1, 0.2, 0.3, 0.4, 0.5, 1, 9 T). (c, d) The temperature dependence of the upper critical field H_{c2} is shown for the 90%, 50% and 10% normal state ρ for $La_{0.85}Th_{0.15}OBiS_2$ and $La_{0.8}Hf_{0.2}OBiS_2$ samples, respectively [12].

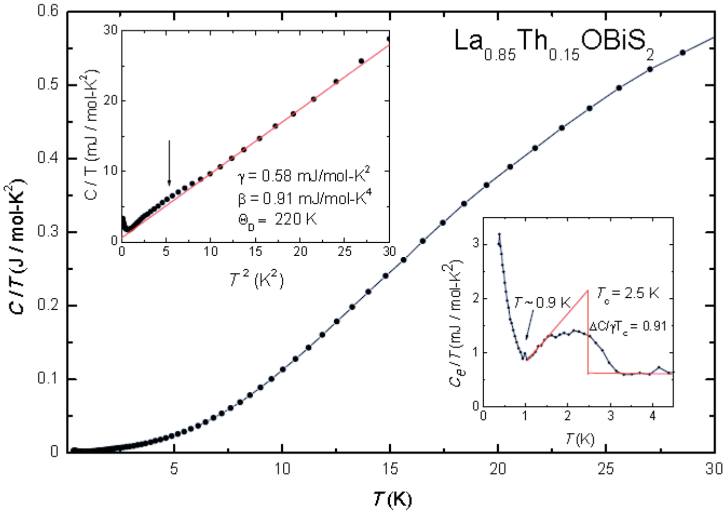

Figure VI.3: Specific heat C divided by temperature T, C/T vs. temperature T for $La_{0.85}Th_{0.15}OBiS_2$. C/T vs. T^2 is shown in the inset in the upper left hand part of the figure. The red line is a fit of the expression $C(T) = \gamma T + \beta T^3$ which yields $\gamma = 0.66$ mJ/mol-K^2 and $\Theta_D = 220$ K. The inset in the lower right part of the figure shows a plot of C_e vs. T, where C_e/T is the electronic contribution to the specific heat ($T_c = 2.5$ K) [12].

the C/T vs. T^2 plot is a fit of the expression $C(T) = \gamma T + \beta T^3$ to the data where γ is the electronic specific heat coefficient and β is the coefficient of the lattice contribution. The electronic contribution to the specific heat C_e/T vs. T is shown, which has been obtained by subtracting the lattice contribution βT^3 from $C(T)$. For $La_{0.85}Th_{0.15}OBiS_2$, Fig. VI.3, the best fit yields $\gamma = 0.58$ mJ/mol-K^2, β = 0.91 mJ/mol-K^4, corresponding to a Debye temperature of $\Theta_D = 220$ K and a $T_c = 2.5$ K. The ratio of the jump, $\Delta C/\gamma T_c$ =0.91, was calculated using a jump in C_e/T of 0.53 mJ/mol-K^2, extracted from the entropy conserving construction as seen in the inset in the lower right. Though this value is lower than the predicted BCS value of 1.43, it is similar to what is seen in $LaO_{0.5}F_{0.5}BiS_2$ [11].

The specific heat data for $La_{0.8}Hf_{0.2}OBiS_2$ are displayed between 0.36 K and 30 K in Fig. VI.4. The upper inset highlights the linear fit to the C/T vs.

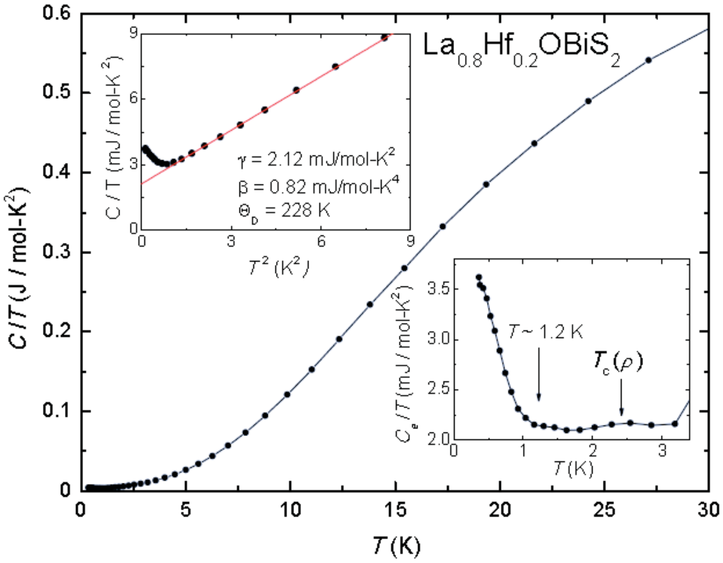

Figure VI.4: C/T vs. temperature T for La$_{0.8}$Hf$_{0.2}$OBiS$_2$. C/T vs. T^2 is shown in the inset in the upper left hand part of the figure. The red line is a fit of the expression $C(T) = \gamma T + \beta T^3$ which yields γ= 2.12 mJ/mol K^2 and Θ_D = 228K. The inset in the lower right shows a plot of C_e vs. T, where C_e/T is the electronic contribution to the specific heat. T_c = 2.36K is indicated by an arrow [12].

T^2, from which we extracted γ = 2.12 mJ/mol-K^2, β = 0.82 mJ/mol-K^4, and Θ_D = 228 K. These data, as can be seen in figures VI.3 and VI.4 measurements have two developments, potentially unaccounted for in other measurements. There is an upturn of an unknown nature in specific heat below roughly 1.2 K and 0.9 K for the La$_{0.8}$Hf$_{0.2}$OBiS$_2$ and La$_{0.85}$Th$_{0.15}$OBiS$_2$ samples, respectively. However, to definitively resolve these mysteries requires further measurements at lower temperatures currently only possible with dilution refrigerators technology. Without access to such technology at that time, the authors suggest this upturn may be a contribution to specific heat from a Schottky anomaly or may be indicative of a second superconducting phase in this compound. There is a second question induced upon inspection of the specific heat data. As can be seen in both figures VI.3 and VI.4 even though a distinct feature resides where the superconducting transition should be the both data are missing well-defined transitions. The authors suggest the absence is due to sample inhomogeneity and, hopefully, ongoing investigations will clear up any doubts.

It is of personal importance that these specific heat measurements are the first published study of this measurement type to these temperatures on a newly discovered family of compounds. Up to that point in time the Quantum Design He-3 Heat Capacity software had not been released for public consumption. These measurements were taken with the help of Manivannan Naillayan, my supervisor at Quantum Design and were meticulously verified since the option was still officially in development.

Bibliography

[1] V. P. S. Awana, A. Kumar, R. Jha, S. Kumar, A. Pal, Shruti, J. Saha, and S. Patnaik, Solid State Communications **157**, 31-23 (2013); **arXiv:1207.6845** (2012).

[2] K. Deguchi, Y. Mizuguchi, S. Demura, H. Hara, T.Watanabe, S. J. Denholme, M. Fujioka, H. Okazaki, T. Ozaki and H. Takeya, EPL **101** 17004 (2013); **arXiv:1209.3846** (2012).

[3] S. Demura, Y. Mizuguchi, K. Deguchi, H. Okazaki, H. Hara, T. Watanabe, S. J. Denholme, M. Fujioka, T. Ozaki and H. Fujihisa, J. Phys. Soc. Jpn. **82**, 033708 (2013); arXiV:1207.5248 (2012).

[4] R. Jha, A. Kumar, S. K. Singh, and V. P. S. Awana, J. Appl. Phys. **113**, 056102 (2013); **arXiv:1208.5873** (2012).

[5] H. Kotegawa, Y. Tomita, H. Tou, H. Izawa, Y. Mizuguchi, O. Miura, S. Demura, K. Deguchi, and Y. Takano, J. Phys. Soc. Jpn. **81**, 103702 (2012)

[6] B. Li, Z. W. Xing, and G. Q. Huang, EPL **101**, 47002 (2013); **arXiv:1210.1743** (2012).

[7] Y. Mizuguchi, H. Fujihisa, Y. Gotoh, K. Suzuki, H. Usui, K. Kuroki, S. Demura, Y. Takano, H. Izawa, and O. Miura, Phys. Rev. B **86**, 220510(R) (2012).

[8] Y. Mizuguchi, S. Demura, K. Deguchi, Y. Takano, H. Fujihisa, Y. Gotoh, H. Izawa, and O. Miura, J. Phys. Soc. Jap. **81**, 114725 (2012).

[9] M. R. Norman, Physics **1**, 21 (2008)

[10] J. Xing, S. Li, X. Ding, H. Yang, and H.-H. Wen, Phys. Rev. B **86**, 214518 (2012); **arXiv:1208.5000** (2012).

[11] D. Yazici, K. Huang, B. D. White, A. H. Chang, A. J. Friedman, and M. B. Maple, Philos. Mag. **93**, 673 (2012).

[12] D. Yazici, K. Huang, B. D. White, I. Jeon, V. W. Burnett, A. J. Friedman, I. K. Lum, M. Nallaiyan, S. Spagna, M. B. Maple, Phys. Rev. B **87**, 174512 (2013)